

A Predictor Corrector Convex Splitting Method for Stefan Problems Based on Extreme Learning Machines

Siyuan Lang^a, Zhiyue Zhang^{a,*}

^aMinistry of Education Key Laboratory for NSLSCS, School of Mathematical Sciences, Nanjing Normal University, Nanjing, China

Abstract

Solving Stefan problems via neural networks is inherently challenged by the nonlinear coupling between the solutions and the free boundary, which results in a non-convex optimization problem. To address this, this work proposes an Operator Splitting Method (OSM) based on Extreme Learning Machines (ELM) to decouple the geometric interface evolution from the physical field reconstruction. Within a predictor-corrector framework, the method splits the coupled system into an alternating sequence of two linear and convex subproblems: solving the diffusion equation on fixed subdomains and updating the interface geometry based on the Stefan condition. A key contribution is the formulation of both steps as linear least-squares problems; this transforms the computational strategy from a non-convex gradient-based optimization into a stable fixed-point iteration composed of alternating convex solvers. From a theoretical perspective, the relaxed iterative operator is shown to be locally contractive, and its fixed points are consistent with stationary points of the coupled residual functional. Benchmarks across 1D to 3D domains demonstrate the stability and high accuracy of the method, confirming that the proposed framework provides a highly accurate and efficient numerical solution for free boundary problems.

Keywords: Operator splitting method, Stefan problem, Extreme Learning Machines, Predictor Corrector, Convex optimization

2020 MSC: 35R35, 65M12, 65M70, 65K10

1. Introduction

Stefan problems model phase change processes involving moving interfaces and are encountered in a wide range of applications, including alloy solidification and crystal growth [1, 2, 3, 4]. Mathematically, they are formulated as moving boundary problems posed on time-dependent domains. A key feature of such systems is that the interface which separates distinct phases (e.g., solid and liquid) is unknown *a priori* and must be determined as part of the solution. The evolution of the phase interface is controlled by the coupling between the heat equations posed in each subdomain and the interface conditions. In particular, the normal velocity of the interface is determined by the discontinuity of the heat flux across the boundary, commonly referred to as the Stefan condition.

Due to the nonlinearity of the free boundary, analytical solutions are rare and typically limited to ideal one-dimensional configurations, often derived using similarity transformation methods [5, 6, 7, 8]. Consequently, numerical simulation is the primary tool for general problems. Conventional numerical approaches can be broadly classified into interface-tracking and interface-capturing methods. Front tracking schemes [9, 10, 11, 12] explicitly represent the interface using moving meshes or Lagrangian markers, which conform to the boundary geometry. In contrast, fixed-grid methods resolve the moving boundary implicitly. The enthalpy method [13, 14, 15] reformulates the governing equations by incorporating latent heat into a unified energy term. Phase-field formulations [16] approximate the sharp interface with a smooth transition layer governed by an auxiliary variable, while level-set methods [17, 18, 19, 20] embed the interface as the zero contour of a higher-dimensional function. For further numerical approaches to Stefan and free boundary problems, we refer the reader to [21, 22, 23, 24, 25, 26, 27, 28] and the references therein.

*Corresponding author.

Email address: zhangzhiyue@njnu.edu.cn (Zhiyue Zhang)

As an alternative to mesh-based discretizations, mesh-free methods based on neural networks have been increasingly investigated for the numerical solution of partial differential equations. Such approaches rely on universal approximation properties [29] to represent the solution by parametric functions and determine the unknown parameters through the minimization of residuals associated with the governing equations. A representative example is the Physics-Informed Neural Network (PINN) framework [30, 31]. PINN-based formulations for Stefan problems [32, 33, 34, 35] typically introduce the moving interface as an additional unknown variable and optimize it together with the solution. To improve computational efficiency, Extreme Learning Machine (ELM)-based approaches [36] have also been adapted to PDE problems. By fixing the hidden-layer parameters and training only the output weights, Physics-Informed ELM (PIELM) methods [37, 38] transform the resulting optimization problem into a convex linear least-squares formulation for linear PDEs. More recently, PIELM schemes have been extended to moving boundary problems [39, 40], where they have demonstrated improved numerical accuracy in interface tracking and temperature approximation. Nevertheless, for Stefan-type problems, the coupling between the evolving interface geometry and the temperature solution remains a fundamental difficulty. When the interface and solution are optimized simultaneously, this nonlinear coupling is reflected in the loss functional, leading to a non-convex optimization problem and limiting the attainable accuracy of both interface reconstruction and solution approximation.

In this work, to address the non-convexity arising in the loss functional associated with coupled interface–solution optimization, we propose an operator splitting method (OSM) formulated within a predictor–corrector framework. Rather than solving the Stefan problem as a fully coupled system, the proposed approach decomposes the interface–field interaction into an alternating iteration, in which the parameters of both the interface geometry and the temperature solution are updated sequentially. Specifically, starting from a predicted interface parameterization, the solution is computed by solving linear heat diffusion equations on fixed subdomains determined by the current interface iteration. Based on the gradients of the solution, the interface parameters are then updated through the Stefan flux condition, yielding an updated set of interface parameters. This alternating procedure naturally defines a Picard-type fixed-point iteration for the interface parameters. Under this operator splitting strategy, the solution reconstruction step and the geometry update step are treated as separate subproblems. Owing to the linear parameterization adopted for both the temperature solution and the interface geometry, each subproblem can be formulated as a linear least-squares problem. We further show that, with an appropriately chosen relaxation factor ρ , the resulting fixed-point iteration constitutes a contraction mapping in a neighborhood of the solution, thereby guaranteeing the local convergence of the alternating iteration. From this perspective, the proposed method transforms the computational task from a non-convex, gradient-based optimization problem induced by interface–solution coupling into a stable fixed-point iteration with alternating convex subproblems. Numerical experiments on benchmark Stefan problems ranging from one to three spatial dimensions demonstrate the accuracy and robustness of the method, including cases exhibiting Mullins–Sekerka instability [41, 24] and Gibbs–Thomson effects.

The remainder of this paper is organized as follows. Section 2 outlines the mathematical formulation of the two-phase Stefan problem and the associated boundary conditions and Stefan conditions. Section 3 presents the proposed numerical framework, detailing the predictor–corrector strategy, the parameterization of the solution and interface, and the operator splitting algorithm. In Section 4, we provide a theoretical analysis of the resulting fixed-point iteration, focusing on its convergence properties and consistency with the coupled formulation. Section 5 reports a series of numerical experiments that demonstrate the accuracy and robustness of the proposed method. Finally, Section 6 concludes the paper with a summary of the main findings.

2. Problem Formulation

Consider a bounded domain $\Omega \subset \mathbb{R}^d$ with boundary $\partial\Omega$. For any time $t \in (0, T]$, the domain is partitioned into two time-dependent disjoint subdomains $\Omega_1(t)$ and $\Omega_2(t)$ separated by a moving interface $\Gamma(t)$, such that $\Omega = \Omega_1(t) \cup \Omega_2(t) \cup \Gamma(t)$. The interface $\Gamma(t)$ represents the unknown free boundary whose position is determined as part of the solution. Let $u : \Omega \times [0, T] \rightarrow \mathbb{R}$ denote the field variable, and let u_i be the restriction of u to $\Omega_i(t)$. The two-phase Stefan problem is governed by the following system of partial differential equations:

$$\frac{\partial u_i}{\partial t} - \nabla \cdot (k_i \nabla u_i) = f_i(\mathbf{x}, t) \quad \text{in } \Omega_i(t), \quad i = 1, 2, \quad (1)$$

subject to the initial conditions $u(\mathbf{x}, 0) = u_0(\mathbf{x})$ and $\Gamma(0) = \Gamma_0$, and boundary conditions on the fixed boundary $\partial\Omega$. At the free boundary $\Gamma(t)$, the solution must satisfy the continuity condition

$$u_1(\mathbf{x}, t) = u_2(\mathbf{x}, t) = 0 \quad \text{on } \Gamma(t). \quad (2)$$

The evolution of $\Gamma(t)$ is driven by the Stefan condition, which relates the normal velocity V_n to the jump in the normal flux across the interface:

$$\beta V_n = [\![k \nabla u]\!] \cdot \mathbf{n} = (k_1 \nabla u_1 - k_2 \nabla u_2) \cdot \mathbf{n} \quad \text{on } \Gamma(t), \quad (3)$$

where β is a strictly positive coefficient, k_i denotes the conductivity of phase i , \mathbf{n} is the unit normal vector on $\Gamma(t)$ pointing from Ω_1 to Ω_2 , and $[\![\cdot]\!]$ denotes the jump operator.

3. Methodology

3.1. Extreme learning machine

To discretize and parameterize the coupled system described in Section 2, we employ the ELM framework [36], which can be interpreted as a class of Random Feature Methods (RFM) [42]. Within this formulation, both the solution fields and the evolving interface are represented by a single-hidden-layer parametric ansatz with randomized and frozen parameters, while only the linear output coefficients are treated as unknowns. The resulting representation is illustrated in Fig. 1.

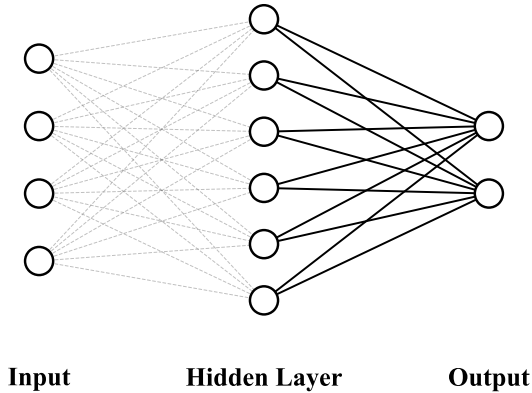


Figure 1: ELM Architecture

We approximate the solution $u_i(\mathbf{x}, t)$ in each phase ($i = 1, 2$) separately. Let $\mathbf{z} = (\mathbf{x}, t) \in \mathbb{R}^{d+1}$ denote the space–time coordinate vector. The approximate solution, denoted by u_i^N , is constructed as a linear expansion of N basis functions:

$$u_i(\mathbf{x}, t) \approx u_i^N(\mathbf{x}, t; \boldsymbol{\beta}_i) = \sum_{j=1}^N \beta_{i,j} \sigma(\mathbf{w}_{i,j} \cdot \mathbf{z} + b_{i,j}) = \boldsymbol{\Phi}_i(\mathbf{x}, t) \boldsymbol{\beta}_i, \quad (4)$$

where $\boldsymbol{\beta}_i = [\beta_{i,1}, \dots, \beta_{i,N}]^\top \in \mathbb{R}^N$ denotes the vector of unknown coefficients. The parameters $\mathbf{w}_{i,j} \in \mathbb{R}^{d+1}$ and $b_{i,j} \in \mathbb{R}$ are drawn from a fixed probability distribution and remain frozen throughout the computation.

The feature map $\boldsymbol{\Phi}_i(\mathbf{x}, t) = [\phi_{i,1}(\mathbf{x}, t), \dots, \phi_{i,N}(\mathbf{x}, t)]$ is defined by $\phi_{i,j}(\mathbf{z}) = \sigma(\mathbf{w}_{i,j} \cdot \mathbf{z} + b_{i,j})$. In this work, we choose the sine activation function $\sigma(z) = \sin(z)$, which yields a randomized Fourier-type trial space suitable for

approximating smooth solutions [43]. With the internal parameters fixed, the action of any linear differential operator \mathcal{L} on u_i^N is linear with respect to the coefficient vector β_i , i.e.,

$$\mathcal{L}[u_i^N](\mathbf{x}, t) = (\mathcal{L}[\Phi_i](\mathbf{x}, t))\beta_i. \quad (5)$$

3.2. Operator splitting method and alternating iteration

To address the coupling and non-linearity associated with the free interface, we propose a framework based on the OSM, as depicted in Figure 2. Instead of solving the coupled system monolithically, this strategy algorithmically decomposes the problem into an alternating iterative sequence of two linear subproblems. Crucially, under the proposed ELM framework introduced in Section 3.1, the update to the parameter of both solution and interface are formulated as Linear Least Squares problems. Consequently, these decoupled steps become convex optimization subproblems. By freezing the interface geometry during the solution solve and subsequently updating the geometry parameter via Stefan condition based on the computed fluxes, we transform the original non-linear optimization task into an alternating predictor-corrector loop. Physically, this method can also be characterized as an iterative thermo-kinematic splitting process.

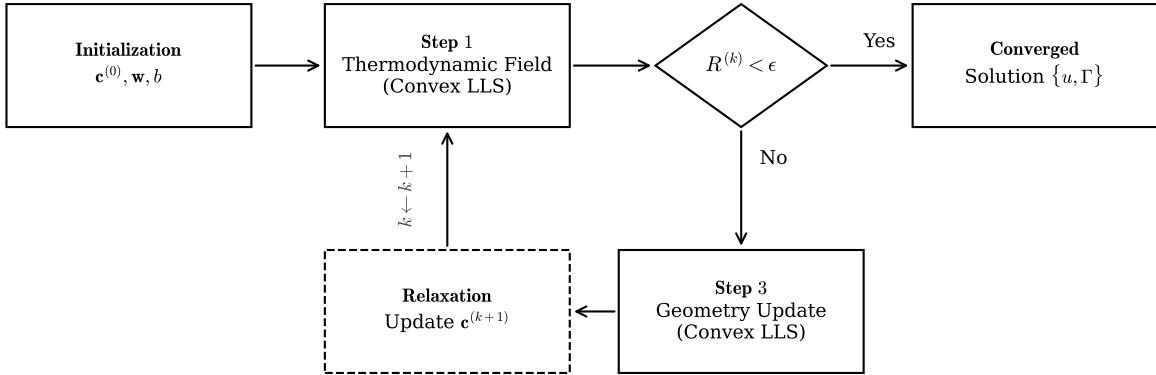


Figure 2: Schematic diagram of the proposed operator splitting framework.

We first parameterize the evolving interface $\Gamma(\cdot, t)$ and the field solution u_i using a linear combination of smooth basis functions. Let the geometry be represented by a parameter vector $\mathbf{c} \in \mathbb{R}^M$ and the solution be represented by β_i , $i = 1, 2$, such that the interface location and field solution are defined by functions

$$\Gamma(\mathbf{x}, t; \mathbf{c}) = \sum_{m=1}^M c_m \Psi_m(\mathbf{x}, t), \quad u_i(\mathbf{x}, t; \beta_i) = \sum_{j=1}^N \beta_{i,j} \Phi_j(\mathbf{x}, t),$$

Here, $\{\Psi_m\}_{m=1}^M$ and $\{\Phi_j\}_{j=1}^N$ are sets of randomized basis functions, specifically $\Psi_m(\mathbf{x}, t) = \sigma(\mathbf{w}_m \cdot (\mathbf{x}, t) + b_m)$, where the internal weights \mathbf{w}_m and biases b_m are randomly initialized and frozen before iteration. The problem then reduces to finding the optimal coefficients $\mathbf{c} \in \mathbb{R}^M$ along with the solution weights β_i , $i = 1, 2$.

The iterative procedure begins with an initial guess $\Gamma^{(0)}$ determined by an initial coefficient vector $\mathbf{c}^{(0)} = \{c_m^{(0)}\}_{m=1}^M$. For each iteration step $k \geq 1$, we first tackle the field subproblem. With the interface geometry $\Gamma^{(k-1)} = \Gamma(\mathbf{x}, t; \mathbf{c}^{(k-1)})$ is fixed, the unknown free boundary is temporarily handled as a known internal boundary. Consequently, the original free boundary problem reduces to a system of coupled linear parabolic initial-boundary value equations defined on the determined space-time subdomains $\Omega_1^{(k-1)}$ and $\Omega_2^{(k-1)}$, which are uniquely partitioned by the frozen interface $\Gamma^{(k-1)}$.

We compute the solutions $u_1^{(k)}$ and $u_2^{(k)}$ by minimizing the residuals of the well-posed governing equations:

$$\frac{\partial u_i^{(k)}}{\partial t} - \nabla \cdot (k_i \nabla u_i^{(k)}) = f_i \quad \text{in } \Omega_i^{(k-1)}, \quad (6)$$

$$u_i^{(k)}(\mathbf{x}, 0) = u_{i,0}(\mathbf{x}), \quad \mathcal{B}_i u_i^{(k)} = g_i \text{ on } \partial\Omega, \quad (7)$$

$$u_1^{(k)} = u_2^{(k)} = 0 \quad \text{on } \Gamma^{(k-1)}. \quad (8)$$

Adopting the ELM architecture described in Section 3.1, we parameterize the solution for each phase i as a linear combination of randomized basis functions: $u_i^{(k)}(\mathbf{x}, t) = \sum_{j=1}^N \beta_{i,j}^{(k)} \Phi_j(\mathbf{x}, t)$, where N denotes the number of hidden neurons. Since the basis functions $\Phi_j = \sigma(w_j \cdot (\mathbf{x}, t) + b_j) \in \{\Phi_j\}_{j=1}^N$ are randomized frozen, minimizing the governing equation residuals constitutes a linear least-squares problem with respect to the unknown weight vector $\beta_i^{(k)}$.

To resolve this subproblem numerically, we employ a collocation strategy driven by Monte Carlo sampling. Specifically, given the geometry delineated by the interface coefficients $\mathbf{c}^{(k-1)}$, we generate four distinct sets of collocation points: interior points $\mathcal{D}_{\Omega,i} = \{(\mathbf{x}_m, t_m)\}_{m=1}^{N_\Omega}$ sampled uniformly within the dynamic space-time subdomains $\Omega_i^{(k-1)}$; initial snapshots $\mathcal{D}_{0,i} = \{(\mathbf{x}_m, 0)\}_{m=1}^{N_0}$ distributed within $\Omega_i(0)$; boundary points $\mathcal{D}_{\partial,i} = \{(\mathbf{x}_m, t_m)\}_{m=1}^{N_\partial}$ located on the fixed exterior boundaries $\partial\Omega_{\text{fixed}} \times (0, T]$; and finally, interface points $\mathcal{D}_\Gamma = \{(\mathbf{x}_m, t_m)\}_{m=1}^{N_\Gamma}$ sampled along the trajectory of the frozen interface $\Gamma^{(k-1)}$.

The thermodynamic field weights $\beta_i^{(k)}$ are then determined by minimizing the aggregate squared residuals over these collocation sets. The discrete loss function $\mathcal{L}(\beta_i)$ is defined as:

$$\begin{aligned} \mathcal{L}_{\text{therm}}(\beta_i) = & \frac{1}{N_\Omega} \sum_{\mathbf{z} \in \mathcal{D}_{\Omega,i}} |\partial_t u_i^N(\mathbf{z}) - \nabla \cdot (\alpha_i \nabla u_i^N(\mathbf{z})) - f_i(\mathbf{z})|^2 \\ & + \frac{\lambda_0}{N_0} \sum_{\mathbf{z} \in \mathcal{D}_{0,i}} |u_i^N(\mathbf{z}) - u_{i,0}(\mathbf{z})|^2 + \frac{\lambda_\partial}{N_\partial} \sum_{\mathbf{z} \in \mathcal{D}_{\partial,i}} |\mathcal{B}_i u_i^N(\mathbf{z}) - g_i(\mathbf{z})|^2 \\ & + \frac{\lambda_\Gamma}{N_\Gamma} \sum_{\mathbf{z} \in \mathcal{D}_\Gamma} |u_i^N(\mathbf{z})|^2, \end{aligned} \quad (9)$$

where $\lambda_0, \lambda_\partial, \lambda_\Gamma$ are penalty weights balancing the contribution of different terms. Therefore, the solution weights $\beta_i^{(k)}$ are solved using the least squares method

$$\beta_i^{(k)} = \underset{\beta}{\text{argmin}} \mathcal{L}_{\text{therm}}(\beta_i). \quad (10)$$

Crucially, since the differential operators are linear and the network architecture is linear with respect to β_i , the minimization of Eq. (9) is strictly equivalent to solving an over-determined linear system via the normal equations:

$$\beta_i^{(k)} = \underset{\beta}{\text{argmin}} \|\mathbf{M}_i(\mathbf{c}^{(k-1)})\beta - \mathbf{y}_i\|_2^2 = (\mathbf{M}_i^T \mathbf{M}_i)^{-1} \mathbf{M}_i^T \mathbf{y}_i. \quad (11)$$

The global system matrix $\mathbf{M}_i(\mathbf{c})$ and the target vector \mathbf{y}_i are constructed by stacking the discretized physical constraints, exhibiting the following block structure:

$$\mathbf{M}_i(\mathbf{c}) = \begin{bmatrix} \mathbf{M}_\Omega \\ \mathbf{M}_0 \\ \mathbf{M}_{\partial\Omega} \\ \mathbf{M}_\Gamma \end{bmatrix}_i, \quad \mathbf{y}_i = \begin{bmatrix} \mathbf{f}_i \\ \mathbf{u}_{i,0} \\ \mathbf{g}_i \\ \mathbf{0} \end{bmatrix}. \quad (12)$$

Physically, the constituent blocks enforce distinct constraints on the basis functions. The sub-matrix $\mathbf{M}_\Omega \in \mathbb{R}^{N_\Omega \times N}$ captures the governing PDE operator evaluated at internal points within $\Omega_i(\mathbf{c})$, while $\mathbf{M}_0 \in \mathbb{R}^{N_0 \times N}$ and $\mathbf{M}_{\partial\Omega} \in \mathbb{R}^{N_\partial \times N}$ impose the initial condition at $t = 0$ and the boundary conditions on $\partial\Omega_{\text{fixed}}$, respectively. The final block, $\mathbf{M}_\Gamma \in \mathbb{R}^{N_\Gamma \times N}$, explicitly enforces the homogeneous condition $u = 0$ on the evolving interface $\Gamma(\mathbf{c})$. Given that the total

number of collocation points $N_{col} = N_\Omega + N_0 + N_\partial + N_\Gamma$ is chosen such that $N_{col} \gg N$, the system is reliably over-determined and well-posed in the least-squares sense.

With the updated solutions $u_i^{(k)}$, we proceed to check the consistency of the Stefan condition. Let $V_n^{(k-1)}$ denote the normal velocity implied by the current geometry parameter $\mathbf{c}^{(k-1)}$. We evaluate the residual of the energy balance at the interface:

$$R_{\text{flux}}^{(k)} = \beta V_n^{(k-1)} - \|k \nabla u^{(k)}\| \cdot \mathbf{n}^{(k-1)}. \quad (13)$$

If $\|R_{\text{flux}}^{(k)}\|_{L^2(\Gamma)}$ falls below a prescribed tolerance ϵ , the iteration is terminated, and the current state is accepted as the converged solution.

If convergence is not yet achieved, we perform a geometry update step. To place the geometry update on the same operator-theoretic footing as the thermodynamic step, we introduce the kinematic residual functional \mathcal{L}_{kin} defined by

$$\mathcal{L}_{\text{kin}}(\mathbf{c}; \boldsymbol{\beta}^{(k)}) = \|\beta V_n(\mathbf{c}) - \|k \nabla u^{(k)}\| \cdot \mathbf{n}^{(k-1)}\|_{L^2(\Gamma^{(k-1)})}^2, \quad (14)$$

where $u^{(k)} = u(\boldsymbol{\beta}^{(k)}; \mathbf{x}, t)$ is obtained from the thermodynamic step and $\mathbf{n}^{(k-1)}$ denotes the unit normal vector of the frozen interface $\Gamma^{(k-1)}$.

We then seek an intermediate coefficient vector, denoted by $\tilde{\mathbf{c}}^{(k)}$, which defines a geometry kinematically consistent with the heat flux computed from the field step. Specifically, $\tilde{\mathbf{c}}^{(k)}$ is obtained as the minimizer of the kinematic functional,

$$\tilde{\mathbf{c}}^{(k)} = \underset{\mathbf{c}}{\operatorname{argmin}} \mathcal{L}_{\text{kin}}(\mathbf{c}; \boldsymbol{\beta}^{(k)}). \quad (15)$$

Finally, to stabilize the iteration and ensure the contraction property of the mapping, we update the interface geometry using a relaxation scheme on the parameters:

$$\mathbf{c}^{(k)} = (1 - \rho) \mathbf{c}^{(k-1)} + \rho \tilde{\mathbf{c}}^{(k)}, \quad (16)$$

where $\rho \in (0, 1]$ is a relaxation parameter. The updated vector $\mathbf{c}^{(k)}$ defines the geometry $\Gamma^{(k)}$ used for the subsequent iteration $k + 1$.

Abstractly, the iterative process defined in Algorithm 1 can be viewed as a fixed-point iteration on the discrete geometry parameter space \mathbb{R}^M . The Thermodynamic Step (Step 1) acts as a thermodynamic operator $\mathcal{T} : \mathbb{R}^M \rightarrow \mathbb{R}^{2N}$ that maps the current interface weights \mathbf{c} to the optimal field weights $\boldsymbol{\beta}_i$, i.e.,

$$\boldsymbol{\beta}^{(k)} = (\boldsymbol{\beta}_1^{(k)}, \boldsymbol{\beta}_2^{(k)}) = \mathcal{T}(\mathbf{c}^{(k-1)}).$$

Conversely, the Kinematic Step (Step 3) functions as a kinematic operator $\mathcal{K} : \mathbb{R}^{2N} \rightarrow \mathbb{R}^M$, mapping the field information back onto the geometry manifold, i.e., $\tilde{\mathbf{c}}^{(k)} = \mathcal{K}(\boldsymbol{\beta}^{(k)})$. Therefore, the entire solver is essentially seeking a fixed point for the composite mapping $\mathbf{c} = (\mathcal{K} \circ \mathcal{T})(\mathbf{c})$. The relaxation scheme in Eq. (16) serves as a damped update to ensure the contraction property of this composite operator,

$$\mathbf{c}^{(k)} = (1 - \rho) \mathbf{c}^{(k-1)} + \rho (\mathcal{K} \circ \mathcal{T}) \mathbf{c}^{(k-1)}, \quad (17)$$

the local convergence of which will be formally analyzed in Section 4.

Remark 1. *The accuracy and robustness of the proposed method stem from the structural decomposition of the original coupled problem. In the Stefan problem, the strong coupling between the free boundary Γ and the solution u renders the simultaneous optimization a non-convex problem, often plagued by complex loss landscapes and local minima.*

In contrast, our operator splitting strategy decouples the system into two subproblems—the thermodynamic field reconstruction and the kinematic geometry fitting. Crucially, due to the ELM linear framework, both subproblems are formulated as Linear Least Squares problems, which are strictly convex and possess unique global minima. Consequently, the update scheme (16) acts as a relaxed Picard iteration. This effectively transforms the intractable challenge of non-convex optimization into a manageable issue of ensuring the contraction property. As will be demonstrated in the error analysis in Section 4, an appropriate choice of the relaxation parameter ρ guarantees the convergence of the algorithm within the attraction basin of the true solution.

Algorithm 1 The proposed Operator Splitting Scheme for Two-Phase Stefan Problems

Require: Frozen random parameters $\{(\mathbf{w}_{i,j}, b_{i,j})\}_{j=1}^N$ for $i = 1, 2$; Initial interface coefficients $\mathbf{c}^{(0)}$; Relaxation parameter $\rho \in (0, 1]$; Tolerance ϵ .

- 1: **Initialization:** Set iteration counter $k \leftarrow 0$.
- 2: **while** $k < K_{\max}$ **do**
- 3: $k \leftarrow k + 1$
- 4: *Step 1: Thermodynamic Operator (Field Solution Solve)*
- 5: Generate collocation points in $\Omega_1^{(k-1)}$ and $\Omega_2^{(k-1)}$ defined by $\mathbf{c}^{(k-1)}$.
- 6: **for** $i = 1, 2$ **do**
- 7: Construct linear system matrices \mathbf{M}_i and \mathbf{y}_i based on Eq. (12).
- 8: Solve via linear least squares for output weights:
- 9:
$$\boldsymbol{\beta}_i^{(k)} \leftarrow \operatorname{argmin}_{\boldsymbol{\beta}} \|\mathbf{M}_i \boldsymbol{\beta} - \mathbf{y}_i\|_2^2$$
- 10: **end for**
- 11: *Step 2: Convergence Check*
- 12: Compute normal velocity $V_n^{(k-1)}$ and flux jump $\mathcal{L}^{(k)} = \llbracket k \nabla u^{(k)} \rrbracket \cdot \mathbf{n}$ on $\Gamma^{(k-1)}$.
- 13: Compute residual: $R = \|\beta V_n^{(k-1)} - \mathcal{L}^{(k)}\|_{L^2(\Gamma)}$.
- 14: **if** $R < \epsilon$ **then**
- 15: **break**
- 16: **end if**
- 17: *Step 3: Kinematic Operator (Geometry parameters Update)*
- 18: Solve via linear least squares for intermediate coefficients $\tilde{\mathbf{c}}$ fitting the Stefan condition:
- 19:
$$\tilde{\mathbf{c}} \leftarrow \operatorname{argmin}_{\mathbf{c}} \|\beta V_n(\mathbf{c}; t) - \mathcal{L}^{(k)}\|_{L^2(\Gamma)}^2$$
- 20: Update interface coefficients with relaxation:
- 21:
$$\mathbf{c}^{(k)} \leftarrow (1 - \rho)\mathbf{c}^{(k-1)} + \rho \tilde{\mathbf{c}}$$
- 19: **end while**
- 20: **return** Solution fields $u_1(\cdot; \boldsymbol{\beta}_1^{(k)})$, $u_2(\cdot; \boldsymbol{\beta}_2^{(k)})$ and interface $\Gamma(\cdot, t; \mathbf{c}^{(k)})$.

Remark 2. It is important to note that the convexity of the subproblems is preserved even in more complex physical settings, such as Stefan problems with interfacial thermal (contact) resistance, where the temperature field is discontinuous across the moving interface. In such cases, the classical continuity condition $u_s = u_l$ on $\Gamma(t)$ is replaced by a flux-dependent jump condition, for instance $\llbracket u \rrbracket = -R_{th} k \nabla u \cdot \mathbf{n}$, which introduces an explicit temperature discontinuity at the interface.

Within the proposed splitting framework, this modification transforms the field subproblem into a linear parabolic interface problem. Crucially, once the interface geometry $\Gamma^{(k-1)}$ is fixed, the resulting interface transmission conditions remain linear with respect to the ansatz weights $\boldsymbol{\beta}$. As a consequence, the thermodynamic sub-step—typically formulated as a linear least-squares problem—retains a strictly convex structure, without requiring any modification of the underlying algorithmic architecture.

The numerical experiments presented later in Section 5.4 demonstrate that this structural convexity and robustness persist in the presence of interfacial temperature jumps, confirming the effectiveness of the proposed approach for discontinuous Stefan problems with thermal resistance.

4. Theoretical Analysis

In this section, we provide a theoretical justification for the convergence properties of the proposed operator splitting method. Since the algorithm operates within the discrete parameter space constructed by the Randomized

Functional Approximation, our analysis focuses on the behavior of the iterative sequence in \mathbb{R}^M . The analysis aims to establish that the fixed point of the proposed algorithmic mapping corresponds to a consistent solution of the semi-discretized Stefan problem, and that the relaxation strategy guarantees local convergence.

4.1. Local convergence of the relaxed fixed-point iteration

We begin by formalizing the iterative procedure as a fixed-point problem. Let $\mathcal{T} : \mathbb{R}^M \rightarrow \mathbb{R}^{2N}$ and $\mathcal{K} : \mathbb{R}^{2N} \rightarrow \mathbb{R}^M$ be the Thermodynamic and Kinematic operators defined in Section 3.2, respectively. We define the *composite update operator* as $\mathcal{M} : \mathbb{R}^M \rightarrow \mathbb{R}^M := \mathcal{K} \circ \mathcal{T}$. Thus, finding a solution to the free boundary problem is equivalent to finding a fixed point $\mathbf{c}^* \in \mathbb{R}^M$ such that $\mathcal{M}(\mathbf{c}^*) = \mathbf{c}^*$, after which the field solution parameters are given by $\boldsymbol{\beta}^* = \mathcal{T}(\mathbf{c}^*)$.

To analyze the stability of the relaxation scheme, we introduce the relaxed operator $\mathcal{G}_\rho : \mathbb{R}^M \rightarrow \mathbb{R}^M$, defined as:

$$\mathcal{G}_\rho(\mathbf{c}) = (1 - \rho)\mathbf{c} + \rho\mathcal{M}(\mathbf{c}). \quad (18)$$

The following theorem establishes the local convergence of the sequence $\mathbf{c}^{(k+1)} = \mathcal{G}_\rho(\mathbf{c}^{(k)})$.

Theorem 1 (Local Convergence via Relaxation). *Assume that the composite operator \mathcal{M} is Fréchet differentiable in an open neighborhood $\mathcal{U} \subset \mathbb{R}^M$ of a fixed point \mathbf{c}^* , and that its Jacobian $\mathbf{J}_\mathcal{M}(\mathbf{c}^*)$ has bounded spectral radius. Then, there exists a relaxation parameter $\rho \in (0, 1]$ and a neighborhood $\mathcal{U}^* \subseteq \mathcal{U}$ containing \mathbf{c}^* , such that the relaxed operator \mathcal{G}_ρ is a contraction mapping on \mathcal{U}^* . Specifically, for any initial guess $\mathbf{c}^{(0)} \in \mathcal{U}^*$, the sequence implies:*

$$\|\mathbf{c}^{(k+1)} - \mathbf{c}^*\| \leq L_\rho \|\mathbf{c}^{(k)} - \mathbf{c}^*\|, \quad (19)$$

where $L_\rho < 1$ is the contraction factor. Consequently, the sequence $\{\mathbf{c}^{(k)}\}_{k \geq 0}$ converges linearly to the unique fixed point \mathbf{c}^* .

Proof. First, we analyze the smoothness of the thermodynamic operator \mathcal{T} . Recall that for a given geometry \mathbf{c} , the field weights $\boldsymbol{\beta} = \mathcal{T}(\mathbf{c})$ are obtained by solving the linear least squares problem Eq. (11):

$$\boldsymbol{\beta} = (\mathbf{M}(\mathbf{c})^T \mathbf{M}(\mathbf{c}))^{-1} \mathbf{M}(\mathbf{c})^T \mathbf{y} := \mathbf{M}(\mathbf{c})^\dagger \mathbf{y}. \quad (20)$$

where $\mathbf{M}(\mathbf{c})$ is the global collocation matrix constructed from the basis functions and their derivatives. Under the standard overparameterized setting $N_{\text{col}} \gg N_{\text{basis}}$, together with the almost sure linear independence of the randomized basis functions, the matrix $\mathbf{M}(\mathbf{c})$ has full column rank in a neighborhood of \mathbf{c}^* . Moreover, since the basis functions are smooth, the entries of $\mathbf{M}(\mathbf{c})$ depend smoothly on \mathbf{c} . Consequently, the Moore–Penrose pseudoinverse $\mathbf{M}(\mathbf{c})^\dagger$ is well defined and uniformly bounded, and the mapping $\boldsymbol{\beta} = \mathcal{T}(\mathbf{c})$ is continuously differentiable in a neighborhood of \mathbf{c}^* .

Next, we consider the kinematic operator \mathcal{K} , which updates the interface geometry based on the computed thermal flux. The residual of Stefan flux Eq. (13) depends linearly on the field coefficients $\boldsymbol{\beta}$. The geometry update is obtained by Eq. (15). Since this step is a linear projection, the kinematic operator \mathcal{K} is continuously differentiable with respect to $\boldsymbol{\beta}$.

Combining the above arguments, both the thermodynamic operator \mathcal{T} and the kinematic operator \mathcal{K} are continuously differentiable in a neighborhood of the fixed point \mathbf{c}^* . Consequently, their composition $\mathcal{M} = \mathcal{K} \circ \mathcal{T}$ is continuously differentiable in a neighborhood of \mathbf{c}^* .

Let $\mathbf{J}_\mathcal{M} = \nabla_{\mathbf{c}} \mathcal{M}(\mathbf{c}^*)$ denote the Jacobian of the composite update operator at the fixed point. For the relaxed fixed-point iteration

$$\mathbf{c}^{(k+1)} = (1 - \rho)\mathbf{c}^{(k)} + \rho\mathcal{M}(\mathbf{c}^{(k)}),$$

a first-order Taylor expansion of \mathcal{M} around \mathbf{c}^* yields the linearized error propagation

$$\mathbf{c}^{(k+1)} - \mathbf{c}^* = [(1 - \rho)\mathbf{I} + \rho\mathbf{J}_\mathcal{M}](\mathbf{c}^{(k)} - \mathbf{c}^*) + O(\|\mathbf{c}^{(k)} - \mathbf{c}^*\|^2). \quad (21)$$

Let $\{\lambda_i\}$ denote the eigenvalues of $\mathbf{J}_\mathcal{M}$. The corresponding eigenvalues of the iteration matrix $\nabla \mathcal{G}_\rho = (1 - \rho)\mathbf{I} + \rho\mathbf{J}_\mathcal{M}$ are $\mu_i(\rho) = 1 - \rho + \rho\lambda_i$. Local linear convergence of the iteration requires the spectral radius condition

$$\max_i |\mu_i(\rho)| < 1.$$

Since $\mathbf{J}_\mathcal{M}$ has bounded spectrum, there exists a sufficiently small relaxation parameter $\rho > 0$ such that all eigenvalues $\mu_i(\rho)$ lie strictly within the unit disk. Hence, the relaxed operator \mathcal{G}_ρ defines a contraction mapping in a neighborhood of \mathbf{c}^* , and the fixed-point iteration converges locally and linearly to \mathbf{c}^* . \square

4.2. Consistency with the Monolithic Formulation

To rigorously situate the proposed framework within the broader context of neural PDE solvers, we analyze the relationship between the fixed point of OSM and the solution obtained via monolithic optimization strategies, such as standard PINNs [34] or coupled PIELM approaches [39, 40].

In monolithic approaches, the geometric parameters \mathbf{c} defining the free interface and the weight parameters $\boldsymbol{\beta}$ approximating the solution are optimized simultaneously. The objective is to find the global minimizer of a composite loss function \mathcal{L}_{global} , which aggregates the residuals from the governing equations and boundary conditions:

$$\mathcal{L}_{global}(\mathbf{c}, \boldsymbol{\beta}) = \lambda_{pde} \|\mathcal{R}_{pde}(\mathbf{c}, \boldsymbol{\beta})\|^2 + \lambda_{bc} \|\mathcal{R}_{bc}(\boldsymbol{\beta})\|^2 + \lambda_{ini} \|\mathcal{R}_{ini}(\mathbf{c}, \boldsymbol{\beta})\|^2 + \lambda_{\Gamma} \|\mathcal{R}_{\Gamma}(\mathbf{c}, \boldsymbol{\beta})\|^2 + \lambda_{stefan} \|\mathcal{R}_{stefan}(\mathbf{c}, \boldsymbol{\beta})\|^2. \quad (22)$$

Here, \mathcal{R}_{pde} , \mathcal{R}_{bc} , and \mathcal{R}_{ini} represent the residuals for the equation, boundary conditions, and initial conditions, respectively. The term \mathcal{R}_{Γ} enforces the Dirichlet continuity condition ($u = 0$) on the evolving free interface, while \mathcal{R}_{stefan} enforces the flux Stefan condition. The simultaneous optimization seeks the pair $(\mathbf{c}^*, \boldsymbol{\beta}^*)$ that minimizes this global functional. However, due to the nonlinear coupling between the domain geometry \mathbf{c} and the field solution $\boldsymbol{\beta}$, the optimization landscape of \mathcal{L}_{global} is inherently non-convex, posing significant challenges for gradient-based solvers in locating the global minimum.

The proposed operator splitting method essentially reformulates this non-convex global minimization into a sequence of convex subproblems effectively decoupling the objective function into a thermodynamic part \mathcal{L}_{therm} and a kinematic part \mathcal{L}_{kin} on each iteration k :

$$\mathcal{L}_{therm}(\mathbf{c}^{(k)}, \boldsymbol{\beta}) = \lambda_{pde} \|\mathcal{R}_{pde}\|_{L^2(\Omega_i^{(k)}(t))}^2 + \lambda_{bc} \|\mathcal{R}_{bc}\|_{L^2(\partial\Omega)}^2 + \lambda_{ini} \|\mathcal{R}_{ini}\|_{L^2(\Omega_i^{(k)}(0))}^2 + \lambda_{\Gamma} \|\mathcal{R}_{\Gamma}\|_{L^2(\Gamma^{(k)})}^2, \quad (23)$$

$$\mathcal{L}_{kin}(\mathbf{c}, \boldsymbol{\beta}^{(k)}) = \lambda_{stefan} \|\mathcal{R}_{stefan}(\boldsymbol{\beta}^{(k)}, \mathbf{c})\|_{L^2(\Gamma^{(k)})}^2. \quad (24)$$

In the Thermodynamic Step of our algorithm, for a fixed interface geometry $\mathbf{c}^{(k)}$, the solver determines the field weights $\boldsymbol{\beta}^{(k)}$ by minimizing $\mathcal{L}_{therm}(\mathbf{c}^{(k)}, \boldsymbol{\beta})$. Crucially, under the proposed ELM framework, this step constitutes a linear least-squares problem. Consequently, the resulting solution $\boldsymbol{\beta}^{(k)}$ is not merely a local approximation but the unique global minimizer of the thermodynamic residual functional on the discretization subspace defined by the current geometry ansatz.

Subsequently, the Kinematic Step updates the geometry parameter \mathbf{c} to align with the Stefan condition driven by the computed field, which is equivalent to minimizing the kinematic residual \mathcal{L}_{kin} with respect to \mathbf{c} . When the iterative scheme converges to a fixed point \mathbf{c}^* (where $\mathbf{c}^* = \mathcal{M}(\mathbf{c}^*)$) with the associated field weights $\boldsymbol{\beta}^* = \mathcal{T}(\mathbf{c}^*)$, it implies that the system fulfills two conditions simultaneously: the temperature field is the optimal resolution for the frozen domain geometry, and the domain geometry is stationary with respect to the thermal fluxes. Therefore, the fixed point pair $(\mathbf{c}^*, \boldsymbol{\beta}^*)$ simultaneously minimizes both \mathcal{L}_{therm} and \mathcal{L}_{kin} . This confirms that the fixed point $(\mathbf{c}^*, \boldsymbol{\beta}^*)$ corresponds to a stationary point of the monolithic residual functional restricted to the chosen approximation spaces. Thus, The operator splitting strategy avoids direct optimize of the coupled non-convex loss landscape by replacing it with a sequence of convex subproblems connected through a relaxed fixed-point iteration.

5. Numerical experiments

In this section, we present a series of numerical experiments to assess the accuracy and robustness of the proposed operator splitting method. Unless otherwise stated, all numerical errors are evaluated using relative L^2 norms computed on a set of testing points.

Let $\{(\mathbf{x}_m, t_m)\}_{m=1}^{N_u}$ denote the testing points in the space-time domain, and let $u_{\text{pred}}(\mathbf{x}, t)$ and $u_{\text{exact}}(\mathbf{x}, t)$ be the numerical and exact solutions, respectively. The relative L^2 error of the temperature field is defined as

$$\|e_u\| = \left(\frac{\sum_{m=1}^{N_u} |u_{\text{pred}}(\mathbf{x}_m, t_m) - u_{\text{exact}}(\mathbf{x}_m, t_m)|^2}{\sum_{m=1}^{N_u} |u_{\text{exact}}(\mathbf{x}_m, t_m)|^2} \right)^{1/2}. \quad (25)$$

Similarly, let $\{t_n\}_{n=1}^{N_\Gamma}$ be a set of testing points in time. Denoting by $\Gamma_{\text{pred}}(t)$ and $\Gamma_{\text{exact}}(t)$ the predicted and exact free boundary positions, respectively, the relative L^2 error of the free boundary is defined as

$$\|e_\Gamma\| = \left(\frac{\sum_{n=1}^{N_\Gamma} |\Gamma_{\text{pred}}(t_n) - \Gamma_{\text{exact}}(t_n)|^2}{\sum_{n=1}^{N_\Gamma} |\Gamma_{\text{exact}}(t_n)|^2} \right)^{1/2}. \quad (26)$$

5.1. One-dimensional one-phase Stefan problem

We begin with a benchmark one-dimensional one-phase Stefan problem [44, 34, 39], which serves as a basic validation case for the proposed operator splitting framework. The problem is posed on a time-dependent spatial domain

$$\Omega(t) = \{x \mid 0 \leq x \leq \Gamma(t)\}, \quad t \in (0, 1],$$

where the free boundary $\Gamma(t)$ is unknown and determined as part of the solution.

The governing equation, together with the initial and boundary conditions, is given by

$$\frac{\partial u}{\partial t} - \frac{\partial^2 u}{\partial x^2} = 0, \quad 0 < x < \Gamma(t), \quad t \in (0, 1], \quad (27)$$

$$u(x, 0) = \frac{x^2}{2} + 2x + \frac{1}{2}, \quad 0 \leq x \leq \Gamma(0), \quad (28)$$

$$\frac{\partial u}{\partial x}(0, t) = 2, \quad t \in (0, 1]. \quad (29)$$

At the moving interface $\Gamma(t)$, the temperature satisfies a homogeneous Dirichlet condition, and the interface evolution is prescribed through the Stefan condition,

$$u(0) = 2\sqrt{3}, \quad u(\Gamma(t), t) = 0, \quad \frac{\partial u}{\partial x}(\Gamma(t), t) = \sqrt{3 + 2t}. \quad (30)$$

For this configuration, an exact analytical solution is available and is given by

$$u_{\text{exact}}(x, t) = \frac{x^2}{2} + 2x + \frac{1}{2} + t, \quad \Gamma_{\text{exact}}(t) = 2\sqrt{3 + 2t}.$$

To assess the numerical performance, we compute the absolute errors of both the solution and the free boundary position. Figure 3a shows the absolute error of the free boundary location over the time interval $t \in (0, 1]$. The figure reports the time evolution of $e_\Gamma(t)$ evaluated from the predicted and exact interface positions. The maximum error magnitude observed in the numerical results is approximately $O(10^{-14})$. Figure 3b presents the pointwise absolute error in the space-time domain $(x, t) \in \Omega(t) \times (0, 1]$. The pointwise absolute error in $\Omega(t)$ also remains at the level of 10^{-14} .

Table 1: Comparison of errors for different methods (PINN [34], PIELM [39], and OSM).

Case	PINN		PIELM		OSM	
	u	s	u	s	u	s
Section 5.1	3.92e-04	1.04e-03	3.44e-08	7.39e-07	2.80e-14	3.27e-14
Section 5.2 Case 1	7.34e-04	3.52e-04	1.04e-07	4.26e-08	1.52e-14	3.16e-15
Section 5.2 Case 2	3.39e-04	4.14e-05	3.19e-06	8.15e-07	4.79e-13	3.12e-14
Section 5.3	3.70e-03	3.70e-03	9.40e-06	2.78e-06	4.57e-13	7.18e-14

5.2. One-dimensional two-phase Stefan problem

We next consider one-dimensional two-phase Stefan problems [44, 45, 39] to further examine the robustness of the proposed operator splitting framework. Compared with the one-phase setting, the two-phase formulation involves two solution fields defined on time-dependent subdomains separated by a moving interface, and requires the accurate evaluation of heat fluxes from both sides of the free boundary.

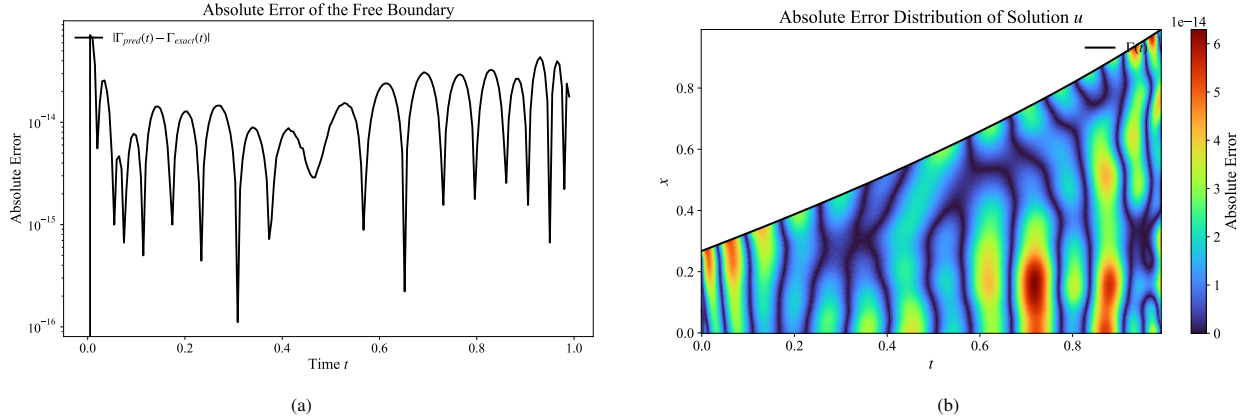


Figure 3: Numerical results for the 1D one-phase Stefan problem. (a) Evolution of the absolute error in the free boundary location $\Gamma(t)$. (b) Heatmap of the pointwise absolute error $|e_u|$ in the space-time domain.

Case 1.

The problem is posed on the fixed time–space domain $(x, t) \in [0, 2] \times [0, 1]$, which is partitioned by a moving interface $\Gamma(t)$ into

$$\Omega_1(t) = \{ 0 \leq x \leq \Gamma(t) \}, \quad \Omega_2(t) = \{ \Gamma(t) \leq x \leq 2 \}.$$

The governing equations for the two phases are given by

$$\frac{\partial u_1}{\partial t} - k_1 \frac{\partial^2 u_1}{\partial x^2} = 0, \quad 0 < x < \Gamma(t), \quad t \in (0, 1], \quad (31)$$

$$\frac{\partial u_2}{\partial t} - k_2 \frac{\partial^2 u_2}{\partial x^2} = 0, \quad \Gamma(t) < x < 2, \quad t \in (0, 1], \quad (32)$$

where $k_1 = 2$ and $k_2 = 1$. The initial and boundary conditions are prescribed as

$$u_1(x, 0) = 2e^{\frac{2x-1}{4}} - 2, \quad u_2(x, 0) = e^{\frac{x-1}{2}} - 1, \quad \Gamma(0) = 0.5, \quad (33)$$

$$u_1(0, t) = 2e^{\frac{2t-1}{4}} - 2, \quad u_2(2, t) = e^{\frac{2t-3}{2}} - 1. \quad (34)$$

At the moving interface $x = \Gamma(t)$, the temperature continuity and Stefan condition are imposed:

$$u_1(\Gamma(t), t) = u_2(\Gamma(t), t) = 0, \quad \frac{d\Gamma}{dt} = \llbracket k \frac{du}{dx} \rrbracket. \quad (35)$$

For this benchmark, the exact solution is given by

$$u_1(x, t) = 2e^{\frac{2t-2x+1}{4}} - 2, \quad u_2(x, t) = e^{\frac{2t-2x+1}{2}} - 1, \quad \Gamma_{\text{exact}}(t) = t + 0.5.$$

The numerical performance for this two-phase scenario is illustrated in Figure 4. Figure 4(a) shows the absolute error of the free boundary position as a function of time. It is observed that the interface error remains at the level of 10^{-14} throughout the entire time interval. Figure 4(b) displays the spatiotemporal distribution of the pointwise absolute error in both phases. The error magnitude is uniformly on the order of 10^{-14} over the space–time domain, including the vicinity of the moving interface.

These results indicate that, for this benchmark, the temperature field and the free boundary are resolved to comparable numerical precision.

Case 2.

We next consider a two-phase Stefan problem defined on the domain $[0, 1.5]$ over the time interval $t \in [0, 1]$. The moving interface $\Gamma(t)$ separates the two phases as

$$\Omega_1(t) = \{ 0 \leq x \leq \Gamma(t) \}, \quad \Omega_2(t) = \{ \Gamma(t) \leq x \leq 1.5 \}.$$

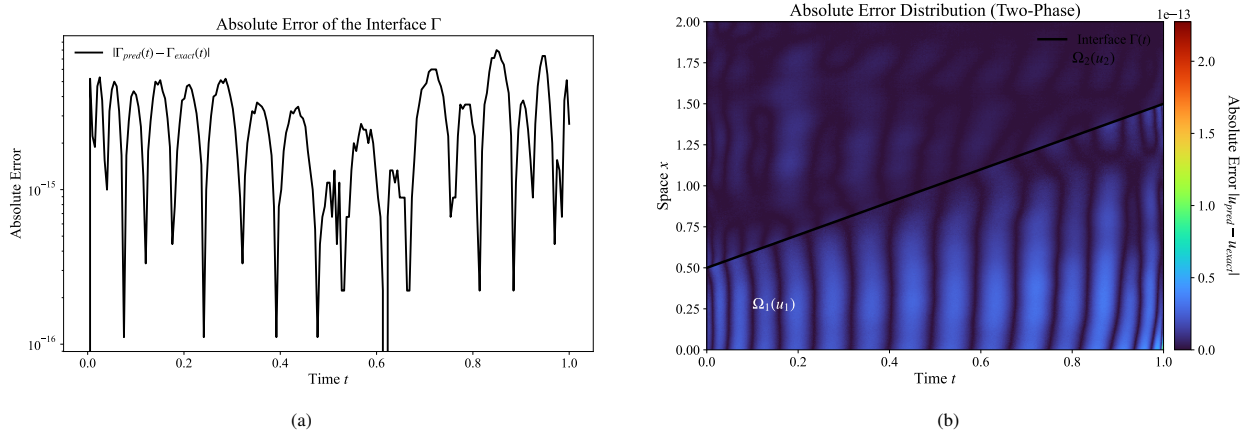


Figure 4: Numerical results for the one-dimensional two-phase Stefan problem (Case 1). (a) Absolute error of the predicted free boundary position $\Gamma(t)$ versus time. (b) Spatiotemporal distribution of the pointwise absolute error $|u_{\text{pred}}(x, t) - u_{\text{exact}}(x, t)|$. The dashed line indicates the exact interface trajectory.

The governing equations are

$$\frac{\partial u_1}{\partial t} - k_1 \frac{\partial^2 u_1}{\partial x^2} = 0, \quad 0 \leq x \leq \Gamma(t), \quad t \in (0, 1], \quad (36)$$

$$\frac{\partial u_2}{\partial t} - k_2 \frac{\partial^2 u_2}{\partial x^2} = 0, \quad \Gamma(t) \leq x \leq 1.5, \quad t \in (0, 1], \quad (37)$$

where $k_1 = 1$ and $k_2 = 1$. The initial and boundary conditions are specified as

$$u_1(x, 0) = 1 - \frac{1}{\text{erf}(\alpha)} \text{erf}\left(\frac{x}{\sqrt{2}}\right), \quad u_2(x, 0) = -1 + \frac{1}{\text{erfc}(\alpha/\sqrt{2})} \text{erfc}\left(\frac{x}{2}\right), \quad (38)$$

$$\Gamma(0) = \alpha \sqrt{2}, \quad (39)$$

$$u_1(0, t) = 1, \quad u_2(1.5, t) = -1 + \frac{1}{\text{erfc}(\alpha/\sqrt{2})} \text{erfc}\left(\frac{1.5}{2\sqrt{2t+1}}\right). \quad (40)$$

At the interface $x = \Gamma(t)$, the continuity and Stefan conditions read

$$u_1(\Gamma(t), t) = u_2(\Gamma(t), t) = 0, \quad \frac{d\Gamma}{dt} = -\frac{\partial u_1}{\partial x} + \frac{\partial u_2}{\partial x}. \quad (41)$$

The parameter α is determined by the transcendental equation

$$\alpha \sqrt{\pi} - \frac{e^{-\alpha^2}}{\text{erf}(\alpha)} + \frac{1}{\sqrt{2}} \frac{e^{-\alpha^2/2}}{\text{erfc}(\alpha/\sqrt{2})} = 0. \quad (42)$$

With the resulting value of α , the exact solutions are given by

$$u_1(x, t) = 1 - \frac{1}{\text{erf}(\alpha)} \text{erf}\left(\frac{x}{\sqrt{4t+2}}\right), \quad (43)$$

$$u_2(x, t) = -1 + \frac{1}{\text{erfc}(\alpha/\sqrt{2})} \text{erfc}\left(\frac{x}{2\sqrt{2t+1}}\right), \quad (44)$$

$$\Gamma_{\text{exact}}(t) = \alpha \sqrt{4t+2}. \quad (45)$$

Figure 6(a) shows the evolution of the predicted interface $\Gamma^{(k)}(t)$ at selected iteration steps. Starting from the initial guess $\Gamma^{(0)}(t) = \Gamma_0$, the interface trajectories at $k = \{0, 1, 2, 5\}$ are displayed and compared with the exact interface

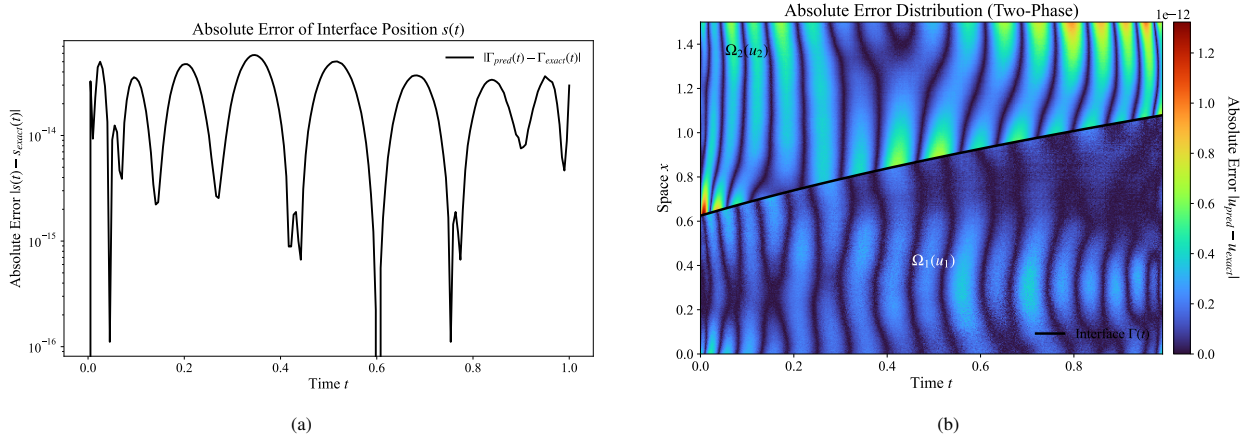


Figure 5: Numerical results for the one-dimensional two-phase Stefan problem (Case 2). (a) Absolute error of the predicted free boundary position $\Gamma(t)$ versus time. (b) Spatiotemporal distribution of the pointwise absolute error $|u_{\text{pred}}(x, t) - u_{\text{exact}}(x, t)|$. The dashed line indicates the exact interface trajectory.

with relaxation factors $\rho = 0.5$. The predicted interfaces progressively approach the exact trajectory as the iteration proceeds. Figure 6(b) reports the convergence histories of the Stefan flux residual $\|\mathcal{R}_{\text{flux}}\|_2$ and the geometric L^2 error $\|\Gamma^{(k)} - \Gamma_{\text{exact}}\|_2$ as functions of the iteration index k with the same relaxation factors. The geometric L^2 error $\|e_{\Gamma}\|_{L^2}$ reach the level of 10^{-13} after approximately 30 iterations.

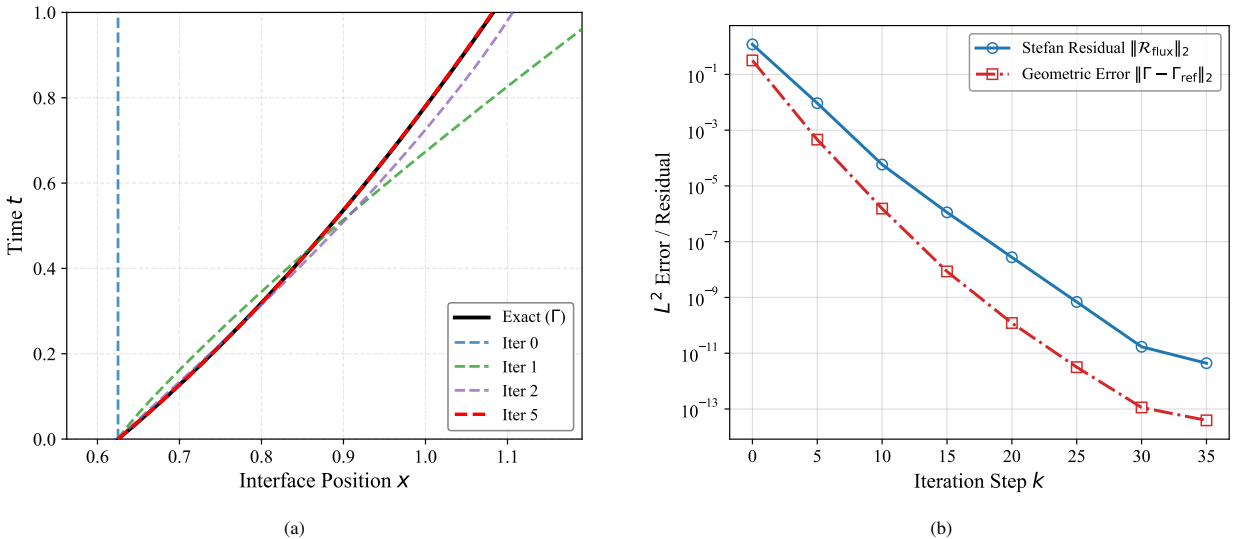


Figure 6: Convergence analysis for the one-dimensional two-phase Stefan problem of $\rho = 0.5$. (a) Evolution of the predicted free boundary trajectory $s^{(k)}(t)$ at selected iteration steps $k = \{0, 2, 5, 10, 50\}$. (b) Convergence history of Stefan flux residual $\|\mathcal{R}_{\text{flux}}\|_2$ and the geometric L^2 error relative to the exact interface.

Figure 7 shows the convergence histories of the geometric L^2 error $\|\Gamma^{(k)} - \Gamma_{\text{exact}}\|_2$ for several values of the relaxation parameter ρ . For all tested values of ρ , the geometric error decreases monotonically with respect to the iteration k . On the semi-logarithmic scale, the error curves exhibit approximately linear decay over a range of iterations, indicating a consistent reduction of the interface error per iteration. Different choices of ρ lead to distinct convergence rates. Larger values of ρ result in steeper initial slopes of the error curves, while smaller values correspond to a more gradual decay. In all cases, the geometric error is reduced to the level of 10^{-13} within a finite number of iterations. This figure illustrates the influence of the relaxation parameter on the iterative convergence behavior of the interface

update.

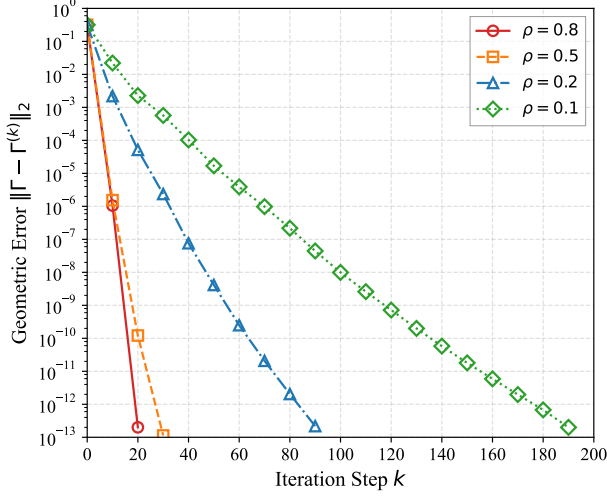


Figure 7: Convergence curves with different relaxation factors ρ

5.3. Two-dimensional two-phase Stefan problem

We next consider a two-dimensional two-phase problem [34, 39] to assess the numerical behavior. The computational domain is the rectangle $\Omega = [0, 2] \times [0, 1]$, which is separated by a moving interface $x = \Gamma(y, t)$ into two subdomains,

$$\Omega_1(t) = \{0 \leq x \leq \Gamma(y, t)\}, \quad \Omega_2(t) = \{\Gamma(y, t) \leq x \leq 2\}.$$

The solution u_1 and u_2 in the two phases are governed by heat equations with distinct diffusivities:

$$\frac{\partial u_1}{\partial t} - k_1 \left(\frac{\partial^2 u_1}{\partial x^2} + \frac{\partial^2 u_1}{\partial y^2} \right) = 0, \quad \text{in } \Omega_1(t), \quad t \in (0, 1], \quad (46)$$

$$\frac{\partial u_2}{\partial t} - k_2 \left(\frac{\partial^2 u_2}{\partial x^2} + \frac{\partial^2 u_2}{\partial y^2} \right) = 0, \quad \text{in } \Omega_2(t), \quad t \in (0, 1]. \quad (47)$$

where $k_1 = 2$ and $k_2 = 1$. The initial conditions for the solution and the interface position are given by

$$u_1(x, y, 0) = 2e^{\frac{1-2x}{4}} - 2, \quad u_2(x, y, 0) = e^{\frac{1-2x}{2}} - 1, \quad \Gamma(y, 0) = 0.5. \quad (48)$$

Time-dependent Dirichlet boundary conditions are imposed on the fixed boundaries

$$u_1(0, y, t) = 2e^{\frac{2y+1}{4}} - 2, \quad u_2(2, y, t) = e^{\frac{2y-3}{2}} - 1, \quad (49)$$

$$u_1(x, 0, t) = u_1(x, 1, t) = 2e^{\frac{2t-2x+1}{4}} - 2, \quad 0 \leq x \leq \Gamma(y, t), \quad (50)$$

$$u_2(x, 0, t) = u_2(x, 1, t) = e^{\frac{2t-2x+1}{2}} - 1, \quad \Gamma(y, t) \leq x \leq 2. \quad (51)$$

On the moving interface $x = s(y, t)$, the temperature is continuous,

$$u_1 = u_2 = 0.$$

The interface evolution is governed by the Stefan condition, which enforces the balance of normal heat fluxes across the interface. For an interface represented as a graph $x = \Gamma(y, t)$, this condition can be written as

$$2 \left(\frac{\partial u_1}{\partial x} - \frac{\partial u_1}{\partial y} \frac{\partial s}{\partial y} \right) - \left(\frac{\partial u_2}{\partial x} - \frac{\partial u_2}{\partial y} \frac{\partial s}{\partial y} \right) = \frac{\partial s}{\partial t}, \quad \text{for } x = \Gamma(y, t). \quad (52)$$

This problem admits an exact solution given by

$$u_1(x, y, t) = 2e^{(2t-2x+1)/4} - 2, \quad u_2(x, y, t) = e^{(2t-2x+1)/2} - 1,$$

with a planar interface

$$s(y, t) = t + 0.5.$$

Figure 8 shows the pointwise absolute error $|u_{\text{pred}} - u_{\text{exact}}|$ at three representative time instances $t = 0.20, 0.50, 0.90$. The moving interface separates the computational domain into two subdomains corresponding to the two phases. As illustrated in the figure, the error magnitude in both phases is on the order of 10^{-12} and the error level remains comparable in the regions of each phase.

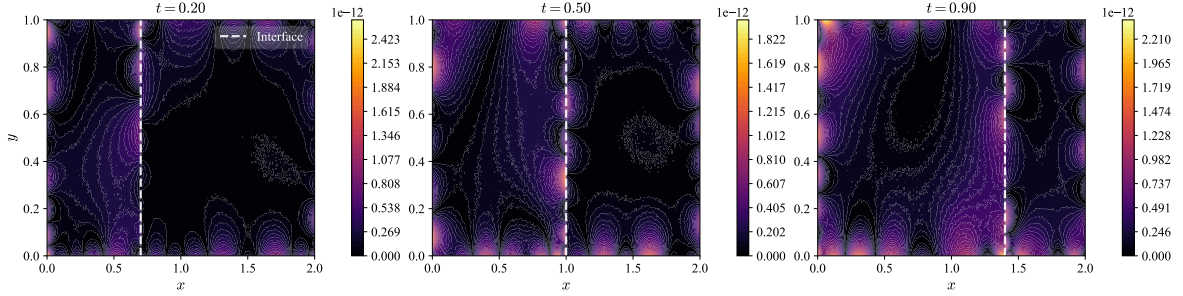


Figure 8: Snapshots of the pointwise absolute error distribution $|u - u_{\text{exact}}|$ at $t = 0.20, 0.50, 0.90$. The moving interface (black dashed line) separates the two phases, and the error remains uniformly low across both subdomains.

To quantify the global accuracy, Figure 9(a) presents the temporal evolution of the relative L^2 error of the solution. The relative L_2 error remains on the level of 10^{-13} throughout the time interval. Figure 9(b) displays the time-space evolution of the free boundary $\Gamma(y, t)$. The surface plot represents the numerical interface position, while the color map indicates the absolute geometric error. As illustrated by the color scale, the absolute geometric error on the interface remains at the level of 10^{-13} over the entire space-time domain.

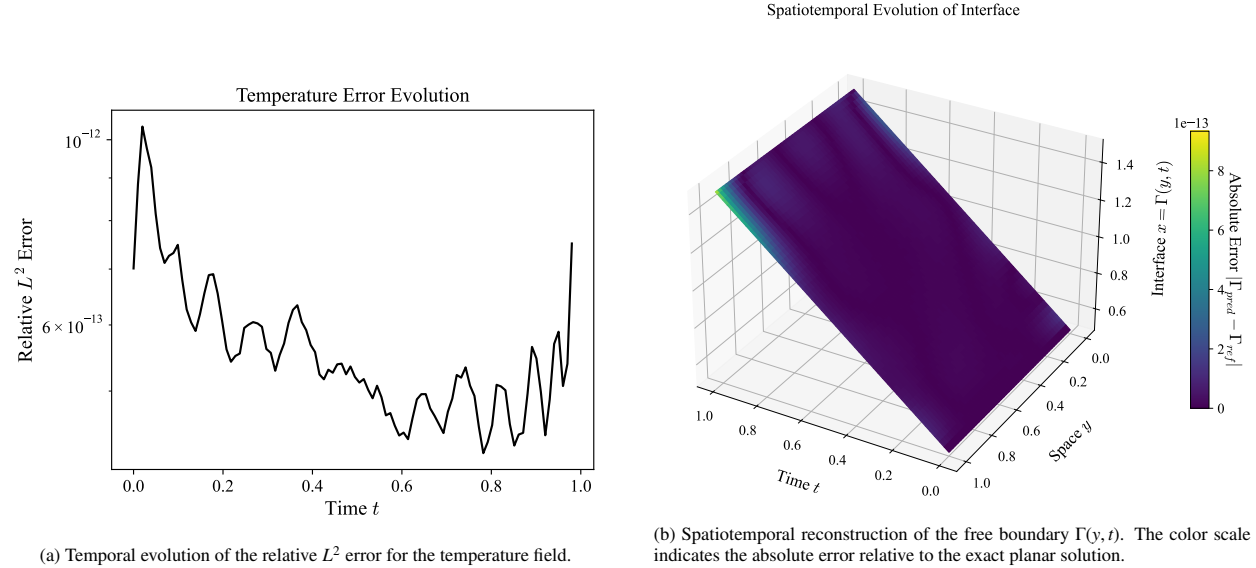


Figure 9: (a) Convergence history of the proposed method, showing stable L^2 error decay. (b) 3D visualization of the interface trajectory and error distribution.

These results demonstrate that the proposed method accurately resolves both the solution and the moving interface in a two-dimensional two-phase stefan problem.

5.4. Stefan problem with thermal resistance

In this subsection, we consider a two-phase Stefan problem with interfacial thermal resistance in a two-dimensional domain $\Omega \subset \mathbb{R}^2$. The domain is separated by a moving interface $\Gamma(t)$ into a solid region $\Omega_s(t)$ and a liquid region $\Omega_l(t)$. The temperature field $u(\mathbf{x}, t)$ satisfies the heat equation in each phase, coupled through a Stefan condition and an imperfect thermal contact condition at the interface.

The governing equations are given by

$$\begin{cases} \rho c_p \frac{\partial u}{\partial t} - \nabla \cdot (k \nabla u) = 0, & \text{in } \Omega \setminus \Gamma(t), \\ \rho L V_n = k_s \frac{\partial u_s}{\partial \mathbf{n}} - k_l \frac{\partial u_l}{\partial \mathbf{n}}, & \text{on } \Gamma(t), \\ u_l - u_s = R_{th} k_l \frac{\partial u_l}{\partial \mathbf{n}}, & \text{on } \Gamma(t), \\ u_l = g_l, \quad u_s = g_s, & \text{on } \partial\Omega \times [0, T], \\ u_l(\mathbf{x}, 0) = u_{0l}, \quad u_s(\mathbf{x}, 0) = u_{0s}, & \mathbf{x} \in \Omega. \end{cases} \quad (53)$$

Here, ρ , c_p , and k denote the density, specific heat capacity, and thermal conductivity, respectively, and L is the latent heat of fusion. The unit normal vector \mathbf{n} is oriented from the solid phase Ω_s toward the liquid phase Ω_l , and V_n denotes the normal velocity of the moving interface. The third equation models the temperature jump $\llbracket u \rrbracket = u_l - u_s$ induced by the interfacial thermal resistance R_{th} .

The computational domain is chosen as $\Omega = [0, 1] \times [0, 1]$. Unless otherwise stated, all physical parameters are set to unity, i.e., $L = \rho = c_p = 1$ and $k_s = k_l = 1$, while the thermal resistance R_{th} is varied.

To facilitate quantitative validation, we consider a planar traveling-wave solution. Let

$$\xi(\mathbf{x}, t) = \frac{x + y}{\sqrt{2}} - Vt$$

denote the coordinate along the propagation direction, so that the interface is located at $\xi = 0$. The exact temperature field is given by

$$u(\mathbf{x}, t) = \begin{cases} 0, & \xi(\mathbf{x}, t) < 0 \quad (\text{solid phase}), \\ T_\infty + \frac{L}{c_p} \exp\left(-\frac{\rho c_p V}{k_l} \xi(\mathbf{x}, t)\right), & \xi(\mathbf{x}, t) \geq 0 \quad (\text{liquid phase}), \end{cases} \quad (54)$$

where the far-field temperature T_∞ is determined from the jump condition as

$$T_\infty = L \left(R_{th} V - \frac{1}{c_p} \right). \quad (55)$$

To assess the pointwise accuracy of the numerical solution, we first examine the spatial distribution of the absolute temperature error $|u_{\text{pred}} - u_{\text{ref}}|$. Figure 10 shows error snapshots at three representative time instances $t \in \{0.2, 0.5, 0.9\}$. The error remains uniformly small throughout the domain, with magnitudes on the order of 10^{-10} .

The main difficulty of this benchmark lies in the accurate treatment of the interfacial temperature discontinuity induced by the thermal resistance R_{th} . In the proposed framework, the discontinuous Stefan problem is decomposed into a sequence of linear parabolic interface subproblems that retain a convex optimization structure. This formulation provides intrinsic robustness with respect to interfacial jumps and enables stable resolution of thermal resistance effects without introducing spurious oscillations. Figure 11 presents three-dimensional visualizations of the predicted temperature field, where a clear separation between the solid (blue) and liquid (red) phases is observed. The sharp temperature jump at the moving interface $x = s(y, t)$ is well preserved throughout the evolution.

Figure 12 depicts the temporal evolution of the relative L^2 error of the temperature field over the time interval $t \in [0, T]$. The error remains stable in time and does not exhibit noticeable accumulation, indicating the robustness of the time-marching procedure for this parabolic free boundary problem.

Finally, the reconstruction of the free boundary manifold is shown in Figure 13. The interface trajectory $\Gamma = \{(x, y, t) \mid x = s(y, t)\}$ is visualized in the space-time domain, with the surface color indicating the relative geometric error $|s_{\text{pred}} - s_{\text{ref}}|/|s_{\text{ref}}|$. The interface position is recovered with near-machine precision, confirming the accurate enforcement of the Stefan condition and the interfacial jump relation.

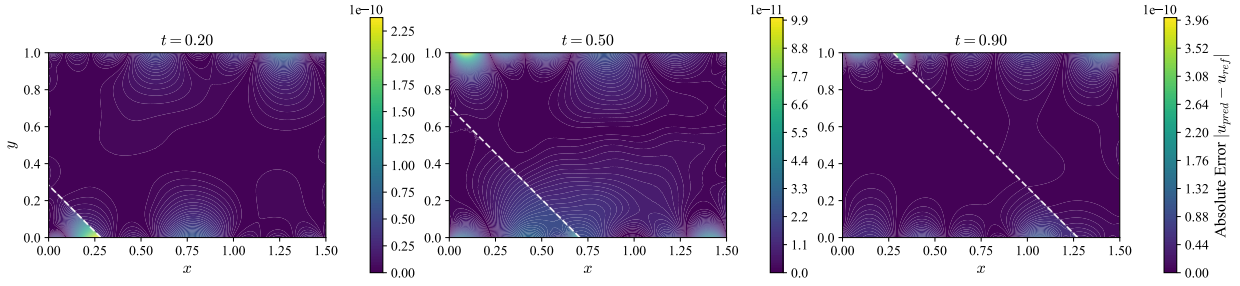


Figure 10: Spatial distribution of the absolute error $|u_{pred} - u_{ref}|$ at three representative time instances.

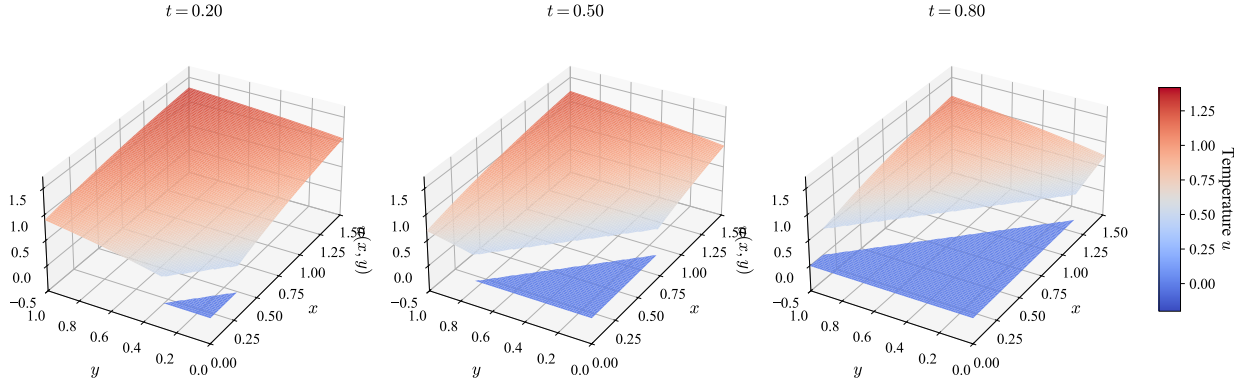


Figure 11: Three-dimensional visualization of the thermal discontinuity (temperature jump) across the interface. The gap between the solid (blue) and liquid (red) surfaces verifies the correct capture of the Stefan condition with thermal resistance.

5.5. Frank sphere problem

In this section, we consider two-dimensional and three-dimensional Frank sphere benchmark problems [46], which admit self-similar analytical solutions.

Case 1. Two-dimensional Frank sphere

We first examine the two-dimensional Frank sphere problem, which describes the radial growth of a solid cylinder $\Omega_s(t)$ into a supercooled liquid region $\Omega_l(t)$. The solution is solved in the liquid phase $\Omega_l(t) = \{(x, y) \in \mathbb{R}^2 \mid r > R(t)\}$, while the solid phase is assumed to remain at the melting temperature u_m .

The governing equations read

$$\begin{cases} \frac{\partial u}{\partial t} = \Delta u, & r > R(t), \quad t > 1, \\ u = u_m, & r = R(t), \\ \lim_{r \rightarrow \infty} u(r, t) = u_\infty, \\ V_n = -\frac{1}{L} \nabla u \cdot \mathbf{n}, & r = R(t), \end{cases} \quad (56)$$

where u denotes the liquid temperature, \mathbf{n} is the outward unit normal pointing into the liquid phase, and V_n is the normal velocity of the interface.

The melting temperature and far-field temperature are fixed as

$$u_m = 0, \quad u_\infty = -1,$$

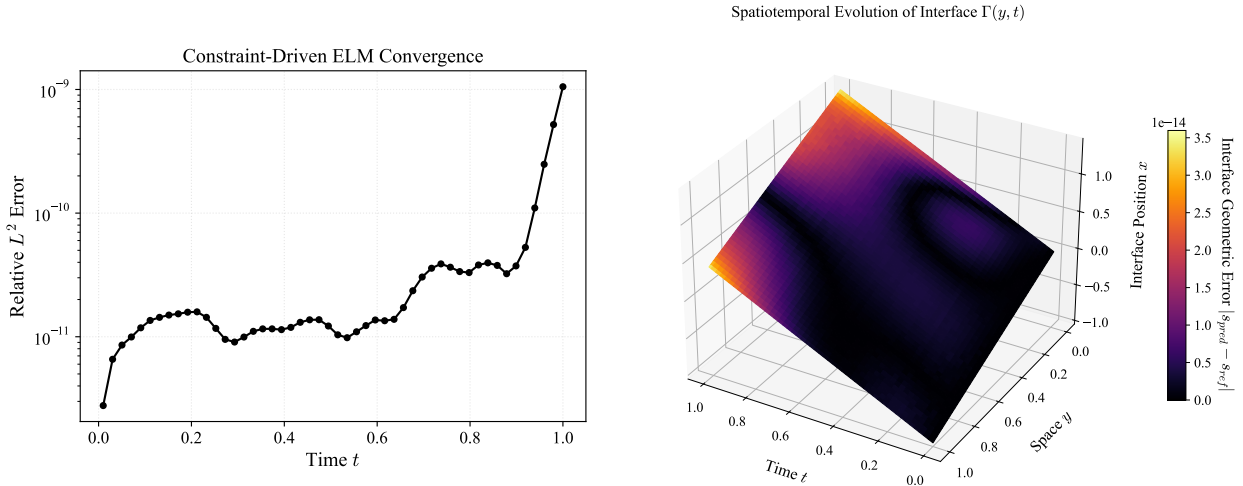


Figure 12: Temporal convergence analysis showing the relative L^2 error of the temperature field in the bulk domain.

Figure 13: Spatiotemporal reconstruction of the free boundary manifold $\Gamma = \{(x, y, t) \mid x = s(y, t)\}$. The color represents the relative geometric error.

and the growth constant is set to $\lambda = 0.5$. The latent heat parameter L is determined consistently from the Stefan condition as

$$L = \frac{u_m - u_\infty}{\lambda^2 e^{\lambda^2} E_1(\lambda^2)},$$

where $E_1(z) = \int_z^\infty \frac{e^{-s}}{s} ds$ denotes the exponential integral function. This problem admits an exact self-similar solution, commonly referred to as the Frank sphere solution, given by

$$u(r, t) = u_\infty + (u_m - u_\infty) \frac{E_1(r^2/4t)}{E_1(\lambda^2)}, \quad r \geq R(t), \quad (57)$$

where $r = \sqrt{x^2 + y^2}$ and $E_1(z) = \int_z^\infty \frac{e^{-s}}{s} ds$ denotes the exponential integral function. The interface radius evolves according to

$$R(t) = 2\lambda \sqrt{t},$$

with the parameter λ determined by a transcendental equation associated with the Stefan number.

In the numerical approximation, the solution on the solid field is represented by the basis expansion

$$u^N(r, t) = \sum_{j=1}^N \beta_j \sigma(\mathbf{w}_j \cdot (r, t) + b_j),$$

where $r = \sqrt{x^2 + y^2}$. The moving interface is approximated by $\Gamma^N(t) = \Gamma(r(\theta, t), t)$.

Numerical results for the two-dimensional Frank sphere problem are shown in Figures 14–16. Figure 14 presents the pointwise absolute error $|u_{\text{pred}} - u_{\text{ref}}|$ at three representative time instances $t = [1.5, 2.0, 3.0]$. The error remains uniformly distributed in the liquid domain, with the maximum magnitude on the order of 10^{-12} .

Figure 15 shows the temporal evolution of the relative L^2 error of the temperature field. The error remains below 10^{-11} over the reported time interval $t \in [1, 3]$ and exhibits a smooth evolution without oscillatory behavior. Figure 16 visualizes the time–space evolution of the free boundary $\Gamma(t)$. The surface is colored by the absolute geometric error on the interface $|\Gamma_{\text{pred}}(t) - \Gamma_{\text{ref}}(t)|$, which remains on the order of 10^{-12} throughout the whole simulation.

Case 2. Three-dimensional Frank sphere

We next consider the three-dimensional Frank sphere problem, which describes a spherical crystal growing into a supercooled liquid from a solid field. The problem is radially symmetric, and the liquid phase occupies the exterior

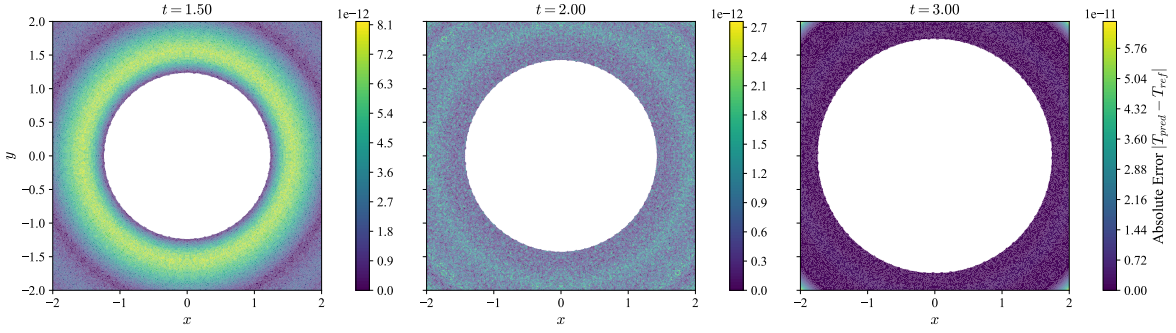


Figure 14: Snapshots of the absolute error distribution of the temperature field at $t = 1.50$, $t = 2.00$, and $t = 3.00$. The white dashed line indicates the moving interface $\Gamma(t)$.

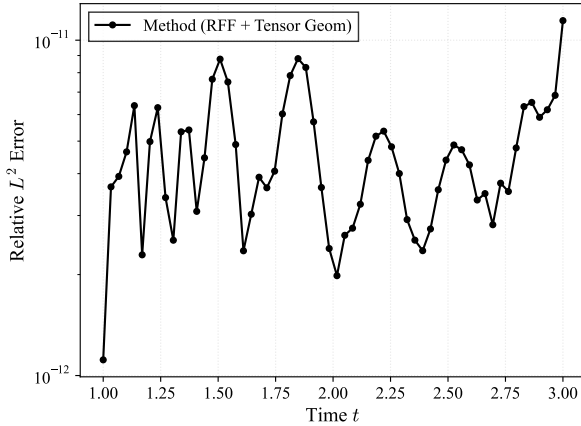


Figure 15: Time evolution of the relative L^2 error in the liquid domain. The stable trend confirms the robustness of the solver.

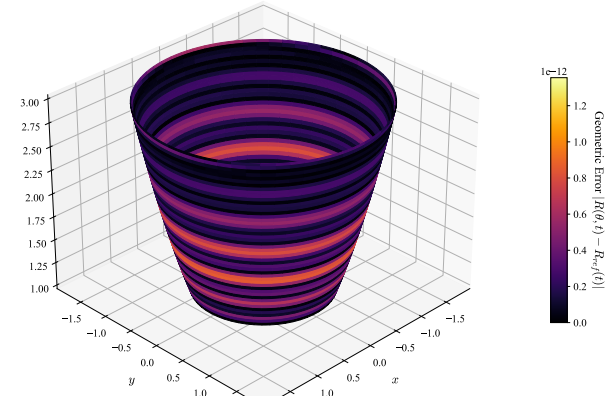


Figure 16: Spatiotemporal evolution of the free boundary $\Gamma(t)$ in the (x, y, t) space. The color map represents the geometric radial error.

region

$$\Omega(t) = \{ \mathbf{x} \in \mathbb{R}^3 \mid \|\mathbf{x}\| > R(t) \}.$$

The dimensionless temperature field $u(\mathbf{x}, t)$ in the liquid phase satisfies the heat equation

$$\frac{\partial u}{\partial t} = \Delta u, \quad \mathbf{x} \in \Omega(t), \quad t > 0. \quad (58)$$

On the moving interface $\Gamma(t) = \{ \mathbf{x} \mid \|\mathbf{x}\| = R(t) \}$, the temperature is fixed at the melting temperature,

$$u(\mathbf{x}, t) = u_m = 0, \quad (59)$$

and the interface velocity is governed by the Stefan condition

$$LV_n = -\nabla u \cdot \mathbf{n}, \quad \mathbf{x} \in \Gamma(t), \quad (60)$$

where V_n denotes the outward normal velocity of the interface, \mathbf{n} is the unit normal pointing into the liquid phase, and L is the latent heat. The far-field condition is prescribed as

$$\lim_{\|\mathbf{x}\| \rightarrow \infty} u(\mathbf{x}, t) = u_\infty < 0.$$

This problem admits a classical self-similar solution, known as the Frank sphere solution. The radius of the solid sphere evolves according to

$$R(t) = 2\lambda \sqrt{t}, \quad (61)$$

where $\lambda > 0$ is a constant determined by the Stefan condition. The temperature distribution in the liquid phase is given by

$$u(r, t) = u_\infty + A F\left(\frac{r}{2\sqrt{t}}\right), \quad r = \|\mathbf{x}\| \geq R(t), \quad (62)$$

with

$$F(\eta) = \frac{e^{-\eta^2}}{\eta} - \sqrt{\pi} \operatorname{erfc}(\eta), \quad (63)$$

and the amplitude

$$A = \frac{u_m - u_\infty}{F(\lambda)}.$$

The latent heat L is determined consistently from the Stefan condition as

$$L = -\frac{A}{2\lambda} F'(\lambda) = \frac{-(u_m - u_\infty)}{2\lambda^3} e^{-\lambda^2} [F(\lambda)]^{-1}. \quad (64)$$

In the numerical experiments, we fix the parameters $\lambda = 0.6$, $u_m = 0$, and $u_\infty = -1.0$, and consider the time interval $t \in [1.0, 3.0]$.

Numerical results for the three-dimensional Frank sphere problem are illustrated in Figures 17–19. Figure 17 shows planar slices of the pointwise absolute error $|u_{\text{pred}} - u_{\text{ref}}|$ at three representative time instances. The error remains spatially smooth and radially symmetric, with the magnitude on the order of 10^{-11} .

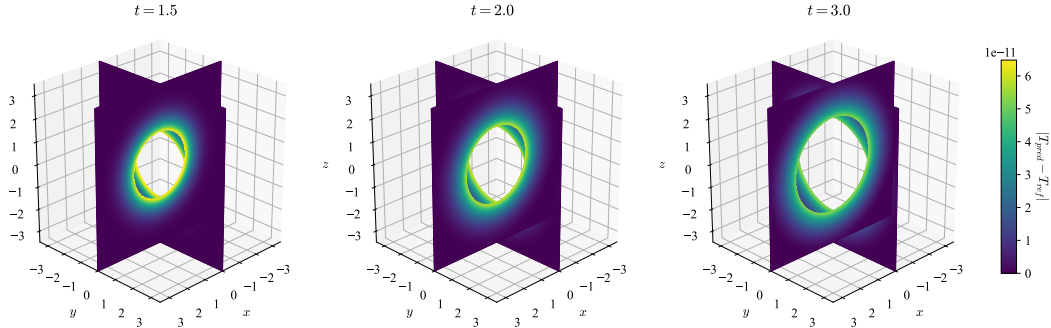


Figure 17: Pointwise absolute error $|u_{\text{pred}} - u_{\text{ref}}|$ for the three-dimensional Frank sphere problem on plane $x = 0$ and $y = 0$ at selected time instances.

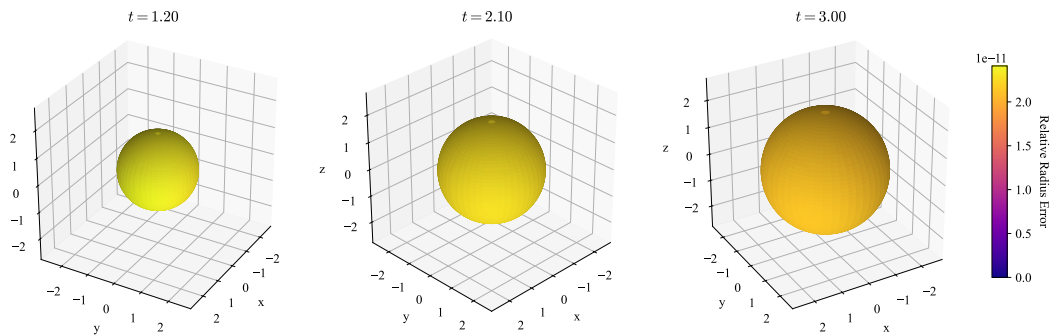


Figure 18: Three-dimensional visualization of the free boundary evolution over time.

Figure 18 visualizes the numerical spherical interface at multiple time levels. The interface geometry follows the exact radial expansion, and the color map indicates the relative radius error, which remains on the order of 10^{-11} throughout the simulation. Figure 19 presents the temporal evolution of the relative L^2 error of the temperature field. The error remains bounded over the entire time interval and exhibits a stable decay trend without oscillatory behavior.

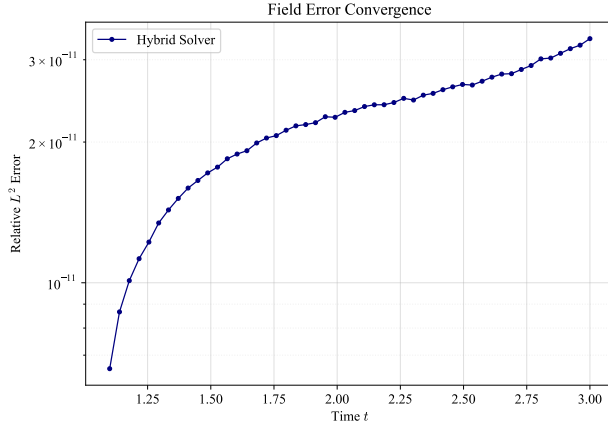


Figure 19: Temporal evolution of the relative L^2 error of the numerical solution for the three-dimensional Frank sphere problem.

5.6. Mullins–Sekerka problem for quasi-stationary Stefan problem

In this section, we consider a two-dimensional Mullins–Sekerka problem arising from the quasi-stationary Stefan model [24]. The liquid domain $\Omega(t)$ is bounded internally by a moving interface $\Gamma(t)$ and externally by a fixed circular boundary Γ_{out} . Under the quasi-stationary assumption, the temperature field $u(r, \theta)$ satisfies the Laplace equation in the bulk, together with a Gibbs–Thomson condition on the interface and a Dirichlet condition on the outer boundary.

The governing equations and kinematic conditions are given by

$$\begin{aligned} \Delta u &= 0, & \text{in } \Omega(t), \\ u(r, \theta) &= u_{\infty}, & \text{on } r = R_{\text{out}}, \\ u(r, \theta) &= -\gamma\kappa, & \text{on } (r, \theta) \in \Gamma(t), \\ V_n &= -\nabla u \cdot \mathbf{n}, & \text{on } \Gamma(t), \end{aligned} \tag{65}$$

where V_n denotes the normal velocity of the interface, \mathbf{n} is the outward unit normal pointing into the liquid phase, and κ denotes the curvature of the interface.

For this benchmark, the far-field temperature is fixed as $u_{\infty} = 1.0$ on the outer boundary located at $R_{\text{out}} = 4.0$. The parameter $\gamma \geq 0$ controls the strength of the curvature (surface tension) effect through the Gibbs–Thomson relation. The initial interface is prescribed as a perturbed circle of the form

$$R(\theta, 0) = R_0 + \delta_0 \cos(k\theta),$$

where δ_0 and k denote the perturbation amplitude and wave number, respectively.

Figure 20 illustrates the evolution of the free boundary for different values of the curvature coefficient γ , with the initial perturbation parameters $\delta_0 = 0.15$ and $k = 5$. As γ increases, the curvature regularization becomes more pronounced, leading to a faster smoothing of high-curvature features and a suppression of sharp interface corners.

6. Conclusion

In this work, we proposed a predictor–corrector operator splitting framework for the numerical solution of Stefan problems, formulated within a randomized functional approximation setting based on Extreme Learning Machines.

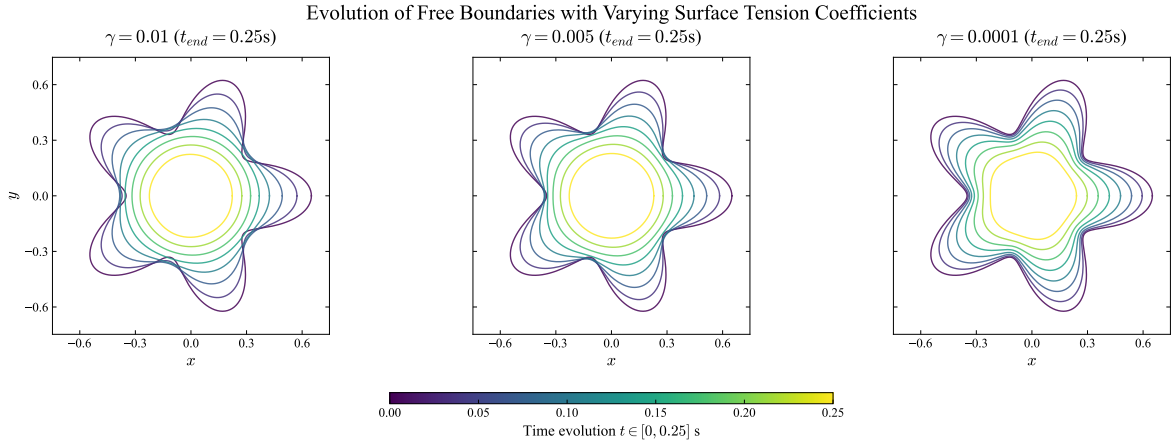


Figure 20: Evolution of the free boundary in the Mullins–Sekerka problem for different values of the surface tension coefficient γ .

The central objective was to address the intrinsic non-convexity arising from the strong coupling between the temperature field and the evolving free boundary when both are treated as optimization variables.

By decomposing the coupled free boundary problem into a thermodynamic subproblem and a kinematic geometry update, the proposed method transforms the original nonlinear optimization into an alternating sequence of linear least-squares problems. Owing to the linear parameterization of both the field and the interface, each subproblem is strictly convex and admits a unique minimizer. From an algorithmic viewpoint, the resulting scheme can be interpreted as a relaxed Picard-type fixed-point iteration on the discrete geometry parameter space, for which local contractivity can be ensured through an appropriate relaxation strategy.

A theoretical analysis was provided to justify the well-posedness of the alternating iteration. In particular, we showed that the thermodynamic and kinematic operators are smooth mappings between finite-dimensional parameter spaces, and that the relaxed composite operator defines a contraction in a neighborhood of the solution. The fixed point of the iteration was shown to be consistent with the optimality conditions of the coupled residual minimization problem restricted to the chosen approximation spaces. This analysis clarifies the mathematical structure underlying the proposed method and distinguishes it from monolithic neural network optimizations, which typically involve non-convex loss landscapes.

Extensive numerical experiments, ranging from one-dimensional to three-dimensional settings, demonstrate that the proposed framework achieves high accuracy and robustness in resolving both the temperature field and the free boundary. The method remains stable across a wide range of benchmark problems, including two-phase Stefan problems, configurations with interfacial thermal resistance, self-similar Frank sphere solutions, and quasi-stationary Mullins–Sekerka instabilities. In all cases, the interface evolution and field reconstruction are resolved with near machine precision, highlighting the effectiveness of the convex splitting strategy.

From a broader perspective, the proposed approach should be viewed as a hybrid numerical method that combines physics-driven operator splitting with randomized functional approximation, rather than as an end-to-end learning paradigm. While the Picard-type iteration yields a linear convergence rate, its stability and convexity properties make it particularly attractive as a refinement or post-processing tool. A natural direction for future work is therefore the development of hybrid workflows, in which a coupled optimization method provides an initial approximation that is subsequently refined by the proposed operator splitting scheme. Further extensions to multi-phase problems, topological interface changes, and adaptive basis enrichment also constitute promising directions for future research.

Acknowledgments

This work was funded by the National Natural Science Foundation of China (grant No. 12571431).

References

- [1] W. J. Boettinger, J. A. Warren, C. Beckermann, A. Karma, Phase-field simulation of solidification, *Annual Review of Materials Research* 32 (2002) 163–194.
- [2] J. S. Langer, Instabilities and pattern formation in crystal growth, *Reviews of Modern Physics* 52 (1980) 1.
- [3] C. Beckermann, Modelling of macrosegregation: applications and future needs, *International Materials Reviews* 47 (2002) 243–261.
- [4] J. A. Sethian, J. Strain, Crystal growth and dendritic solidification, *Journal of Computational Physics* 98 (1992) 231–253.
- [5] A. Briozzo, M. Natale, D. Tarzia, Explicit solutions for a two-phase unidimensional lamé-clapeyron–Stefan problem with source terms in both phases, *Journal of Mathematical Analysis and Applications* 329 (2007) 145–162.
- [6] W. Liu, J. Yao, Y. Wang, Exact analytical solutions of moving boundary problems of one-dimensional flow in semi-infinite long porous media with threshold pressure gradient, *International Journal of Heat and Mass Transfer* 55 (2012) 6017–6022.
- [7] V. Voller, J. Swenson, C. Paola, An analytical solution for a Stefan problem with variable latent heat, *International Journal of Heat and Mass Transfer* 47 (2004) 5387–5390.
- [8] L. Rubinshtein, *The Stefan problem*, volume 27, American Mathematical Soc., 1971.
- [9] D. E. Womble, A front-tracking method for multiphase free boundary problems, *SIAM Journal on Numerical Analysis* 26 (1989) 380–396.
- [10] S. O. Unverdi, G. Tryggvason, A front-tracking method for viscous, incompressible, multi-fluid flows, *Journal of Computational Physics* 100 (1992) 25–37.
- [11] D. Juric, G. Tryggvason, A front-tracking method for dendritic solidification, *Journal of Computational Physics* 123 (1996) 127–148.
- [12] G. Marshall, A front tracking method for one-dimensional moving boundary problems, *SIAM Journal on Scientific and Statistical Computing* 7 (1986) 252–263.
- [13] V. Voller, M. Cross, Accurate solutions of moving boundary problems using the enthalpy method, *International Journal of Heat and Mass Transfer* 24 (1981) 545–556.
- [14] V. Voller, An implicit enthalpy solution for phase change problems: with application to a binary alloy solidification, *Applied Mathematical Modelling* 11 (1987) 110–116.
- [15] A. Date, Novel strongly implicit enthalpy formulation for multidimensional Stefan problems, *Numerical Heat Transfer, Part B Fundamentals* 21 (1992) 231–251.
- [16] J. Mackenzie, M. Robertson, A moving mesh method for the solution of the one-dimensional phase-field equations, *Journal of Computational Physics* 181 (2002) 526–544.
- [17] S. Osher, J. A. Sethian, Fronts propagating with curvature-dependent speed: Algorithms based on hamilton–jacobi formulations, *Journal of Computational Physics* 79 (1988) 12–49.
- [18] F. Gibou, R. Fedkiw, A fourth order accurate discretization for the laplace and heat equations on arbitrary domains, with applications to the Stefan problem, *Journal of Computational Physics* 202 (2005) 577–601.
- [19] J. Papac, A. Helgadottir, C. Ratsch, F. Gibou, A level set approach for diffusion and Stefan-type problems with robin boundary conditions on quadtree/octree adaptive cartesian grids, *Journal of Computational Physics* 233 (2013) 241–261.

[20] L. A. Larios-Cardenas, F. Gibou, Error-correcting neural networks for semi-lagrangian advection in the level-set method, *Journal of Computational Physics* 471 (2022) 111623.

[21] S. Chen, B. Merriman, S. Osher, P. Smereka, A simple level set method for solving Stefan problems, *Journal of Computational Physics* 135 (1997) 8–29.

[22] A. Limare, S. Popinet, C. Josserand, Z. Xue, A. Ghigo, A hybrid level-set/embedded boundary method applied to solidification-melt problems, *Journal of Computational Physics* 474 (2023) 111829.

[23] R. Nürnberg, A structure preserving front tracking finite element method for the mullins–sekerka problem, *Journal of Numerical Mathematics* 31 (2023) 137–155.

[24] T. Eto, A rapid numerical method for the mullins–sekerka flow with application to contact angle problems, *Journal of Scientific Computing* 98 (2024) 63.

[25] J. W. Barrett, H. Garcke, R. Nürnberg, On stable parametric finite element methods for the Stefan problem and the mullins–sekerka problem with applications to dendritic growth, *Journal of Computational Physics* 229 (2010) 6270–6299.

[26] J. Escher, G. Simonett, A center manifold analysis for the mullins–sekerka model, *Journal of Differential Equations* 143 (1998) 267–292.

[27] S. L. Mitchell, T. G. Myers, Application of standard and refined heat balance integral methods to one-dimensional Stefan problems, *SIAM Review* 52 (2010) 57–86.

[28] J. Strain, Linear stability of planar solidification fronts, *Physica D: Nonlinear Phenomena* 30 (1988) 297–320.

[29] G. Cybenko, Approximation by superpositions of a sigmoidal function, *Mathematics of Control, Signals and Systems* 2 (1989) 303–314.

[30] M. Raissi, P. Perdikaris, G. E. Karniadakis, Physics-informed neural networks: A deep learning framework for solving forward and inverse problems involving nonlinear partial differential equations, *Journal of Computational Physics* 378 (2019) 686–707.

[31] C. Fan, S. Lang, M. Toseef, Z. Zhang, A hybrid predictor–corrector decoupled method based on operator learning for solving interface problems, *Journal of Nonlinear Science* (2026) (Preprint).

[32] J. Li, W. Wu, X. Feng, Improved physics-informed neural networks combined with small sample learning to solve two-dimensional Stefan problem, *Entropy* 25 (2023) 675.

[33] B. E. Madir, F. Luddens, C. Lothodé, I. Danaila, Physics informed neural networks for heat conduction with phase change, *International Journal of Heat and Mass Transfer* 252 (2025) 127430.

[34] S. Wang, P. Perdikaris, Deep learning of free boundary and Stefan problems, *Journal of Computational Physics* 428 (2021) 109914.

[35] M. Shkolnikov, H. M. Soner, V. Tissot-Daguette, Deep level-set method for Stefan problems, *Journal of Computational Physics* 503 (2024) 112828.

[36] G. Huang, Q. Zhu, C. Siew, Extreme learning machine: theory and applications, *Neurocomputing* 70 (2006) 489–501.

[37] V. Dwivedi, B. Srinivasan, Physics informed extreme learning machine (PIELM)—a rapid method for the numerical solution of partial differential equations, *Neurocomputing* 391 (2020) 96–118.

[38] S. Dong, Z. Li, Local extreme learning machines and domain decomposition for solving linear and nonlinear partial differential equations, *Computer Methods in Applied Mechanics and Engineering* 387 (2021) 114129.

- [39] F. Ren, P. Zhuang, X. Chen, H. Yu, H. Yang, Physics-informed extreme learning machine (PIELM) for Stefan problems, *Computer Methods in Applied Mechanics and Engineering* 441 (2025) 118015.
- [40] C. Chang, T. Lin, M. Lai, Physics-informed machine learning for two-phase moving-interface and Stefan problems, *ArXiv Preprint ArXiv:2512.14010* (2025).
- [41] R. Sekerka, Stability of a planar interface during solidification of a dilute binary alloy, *Journal of Applied Physics* 35 (1964) 444–451.
- [42] A. Rahimi, B. Recht, Random features for large-scale kernel machines, *Advances in Neural Information Processing Systems* 20 (2007).
- [43] Z. Xia, W. Dai, X. Liu, H. Zhang, X. Ma, Data-specific activation function learning for constructive neural networks, *Neurocomputing* 617 (2025) 129020.
- [44] R. Furzeland, A comparative study of numerical methods for moving boundary problems, *IMA Journal of Applied Mathematics* 26 (1980) 411–429.
- [45] B. T. Johansson, D. Lesnic, T. Reeve, A meshless method for an inverse two-phase one-dimensional linear Stefan problem, *Inverse Problems in Science and Engineering* 21 (2013) 17–33.
- [46] F. C. Frank, Radially symmetric phase growth controlled by diffusion, *Proceedings of the Royal Society of London. Series A. Mathematical and Physical Sciences* 201 (1950) 586–599.